Editors' Suggestion

Coupled structural distortions, domains, and control of phase competition in polar $SmBaMn_2O_6$

Elizabeth A. Nowadnick,[1,2,3,*] Jiangang He,[3,4] and Craig J. Fennie[3]

[1]*Department of Materials Science and Engineering, University of California, Merced, Merced, California 95343, USA*
[2]*Department of Physics, New Jersey Institute of Technology, Newark, New Jersey 07102, USA*
[3]*School of Applied and Engineering Physics, Cornell University, Ithaca, New York 14853, USA*
[4]*Department of Materials Science and Engineering, Northwestern University, Evanston, Illinois 60608, USA*

(Received 28 June 2019; revised manuscript received 2 October 2019; published 18 November 2019)

Materials with coupled or competing order parameters display highly tunable ground states, where subtle perturbations reveal distinct electronic and magnetic phases. These states generally are underpinned by complex crystal structures, but the role of structural complexity in these phases often is unclear. We use group-theoretic methods and first-principles calculations to analyze a set of coupled structural distortions that underlie the polar charge and orbitally ordered antiferromagnetic ground state of *A*-site ordered $SmBaMn_2O_6$. We show that these distortions play a key role in establishing the ground state and stabilizing a network of domain wall vortices. Furthermore, we show that the crystal structure provides a knob to control competing electronic and magnetic phases at structural domain walls and in epitaxially strained thin films. These results provide new understanding of the complex physics realized across multiple length scales in $SmBaMn_2O_6$ and demonstrate a framework for systematic exploration of correlated and structurally complex materials.

DOI: 10.1103/PhysRevB.100.195129

I. INTRODUCTION

Complex materials host multiple coupled or competing structural, electronic, and magnetic order parameters. This complexity manifests itself across multiple length scales. At the microscopic level, the interplay of multiple degrees of freedom plays a key role in correlated electron phases such as metal-insulator transitions in the nickel and vanadium oxides [1], high-temperature superconductivity in the copper oxides [2], and colossal magnetoresistance in the manganese oxides [3,4]. At the mesoscale, complex domain structures involving networks of domain wall vortices and antivortices encode the coupling or competition between multiple order parameters [5,6]. Between these two extremes, individual domain walls can stabilize states distinct from the bulk, such as conducting domain walls in insulators [7–11], local ferromagnetism at domain walls in antiferromagnets [12,13], and the modulation of superconductivity at twin walls [14]. Understanding and ultimately controlling coupled and competing degrees of freedom across this range of length scales remains a challenge.

The rare-earth manganese oxide perovskites provide an ideal context in which to address this challenge because they host several coupled and competing structural, charge order (CO), orbital order (OO), and magnetic phases. We concentrate here on the *A*-site ordered series $RBaMn_2O_6$ (R = rare earth); Fig. 1 shows the experimental phase diagram of this series. As the rare-earth ionic radius increases, the ground state evolves from a CO/OO CE-type antiferromagnetic (CE-AFM) insulator, to an A-type AFM (A-AFM) metal, and finally to a ferromagnetic (FM) metal [15–17]. We focus in particular on $SmBaMn_2O_6$, which in addition to being the closest CO/OO/CE-AFM insulating compound to the phase boundary with the A-AFM and FM metallic systems, also possesses a polar crystal structure [18–22], which enables additional functionality.

The coupled CO/OO/CE-AFM state realized in *A*-site ordered $SmBaMn_2O_6$ is ubiquitous in half-doped manganites, and has been the subject of extensive investigations [3]. $SmBaMn_2O_6$ also has a complex crystal structure characterized by multiple structural distortions that displace the atoms away from their high-symmetry positions. This structural complexity, as well as its interplay with the electronic and magnetic degrees of freedom, remains much less explored. Here, we use group-theoretic methods and density functional theory (DFT)+U calculations to analyze the complex ground-state crystal structure as well as competing metastable structural phases of $SmBaMn_2O_6$. We find that the interplay of multiple symmetry-allowed couplings between structural distortions is key for stabilizing not only the structural, but also the electronic and magnetic ground states. While the role of the electronic and magnetic degrees of freedom in the CO/OO/CE-AFM state is well known, the contribution of the structural couplings to stabilizing this state has not been appreciated in the past.

We then show that the crystal structure is the key "control knob to turn" to realize competing phases and the novel properties associated with them in $SmBaMn_2O_6$. We discuss examples of how to take advantage of this structural control knob across a range of length scales, from single domain thin films, to domain walls in bulk systems. Taken together, our results provide insight into the coupled degrees of freedom in $SmBaMn_2O_6$, and also show an approach to analyzing complex crystal structures and their impact on the correlated charge, orbital, and spin degrees of freedom, which

*enowadnick@ucmerced.edu

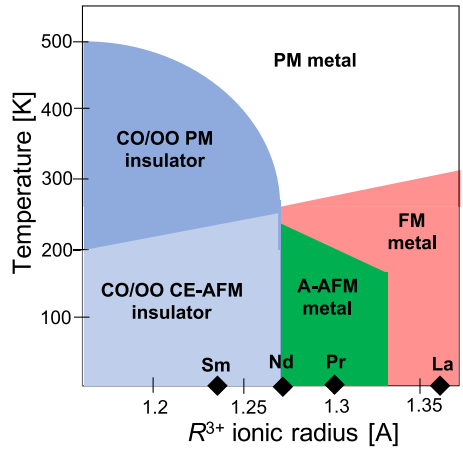

FIG. 1. Experimental phase diagram of the A-site ordered $R\mathrm{BaMn_2O_6}$ family (R = rare earth), adapted from Refs. [15,16]. Here CO = charge order, OO = orbital order, PM = paramagnetic, FM = ferromagnetic, AFM = antiferromagnetic.

is applicable to other systems. In particular, we expect that our analysis also applies to the related $n = 2$ Ruddlesden-Popper $\mathrm{Pr(Sr_{1-x}Ca_x)_2Mn_2O_7}$, which displays an analogous polar CO/OO/CE-AFM ground state [23–25].

The outline for the rest of this paper is as follows. In Sec. II we check that DFT + U provides a satisfactory description of the ground-state physics of $\mathrm{SmBaMn_2O_6}$ for our study. In Sec. III we analyze the crystal structure by decomposing it into symmetry distinct distortions, and we understand the relationship between these distortions via a Landau free-energy expansion in Sec. IV. We then apply this analysis in Sec. V to reveal the relationship between the structure and the electronic/magnetic order, and in Sec. VI to elucidate the ferroelectric mechanism. We analyze the low-energy phases that may compete with the ground state in Sec. VII. In the next sections, we show how the domain structure encodes the coupled and competing degrees of freedom in $\mathrm{SmBaMn_2O_6}$: Sec. VIII analyzes the ground-state domains and enumerates the types of domain walls, Sec. IX shows that the walls organize into a network of domain wall vortices and antivortices, and Sec. X explores scenarios for the competing phases that may be realized at the domain walls. Finally, Sec. XI shows how epitaxial strain can control the ground state and stabilize a competing FM phase. In Sec. XII we summarize our results.

II. REPRODUCING THE GROUND-STATE PROPERTIES

In correlated insulating systems that have competing metallic phases close in energy, the sense in which DFT + U captures the relevant underlying physics must be made clear (see Appendix A for computational methods). In particular, it is critical to check that DFT + U captures both the details of the experimentally observed ground-state crystal structure as well as the observed ground-state charge, spin, and orbital order at the same U value. We use the experimentally reported $R\mathrm{BaMn_2O_6}$ phase diagram shown in Fig. 1 to guide our choice of U value. We select a U such that the computed ground state reproduces the experimentally reported ground-state structural symmetry and magnetic order for several R (see Appendix B). We hold U fixed for the remainder of this work.

TABLE I. Lattice parameters and decomposition of the $P2_1am$ structure obtained from DFT+U and from experiment (Ref. [21]) into symmetry-adapted modes of $P4/mmm$. The amplitudes $\tilde{Q}$ are given for the 40-atom crystallographic unit cell in Å. The positive real numbers $a \neq b$ specify the irrep directions.

Irrep	Wave vector	Direction	Space group	Amplitude	DFT	Expt.
M_5^-	$(\frac{1}{2},\frac{1}{2},0)$	(0,-a)	$Pbmm$	$\tilde{Q}_T$	0.86	0.79
M_4^+	$(\frac{1}{2},\frac{1}{2},0)$	a	$P4/mmm$	$\tilde{Q}_b$	0.20	0.19
Γ_5^-	(0,0,0)	(-a,-a)	$Amm2$	$\tilde{Q}_P$	0.04	0.05
Σ_2	$(\frac{1}{4},\frac{1}{4},0)$	(a, b,0,0)	$P2_1am$	$\tilde{Q}_s$	0.91	0.71

Lattice parameter (Å)	DFT	Expt.
a	11.07	11.10
b	5.53	5.54
c	7.55	7.58

We next summarize the relevant experimentally known properties of $\mathrm{SmBaMn_2O_6}$ and check that our calculations reproduce these properties. Due to the large size mismatch between Sm and Ba, $\mathrm{SmBaMn_2O_6}$ can be stabilized in an A-site ordered double-perovskite form, with Sm and Ba stacking alternately along the c axis. At high temperature, $\mathrm{SmBaMn_2O_6}$ crystallizes in the $Cmmm$ space group, and undergoes two structural-CO/OO transitions as the temperature lowers. At $T_1 = 380$ K, it transitions to a structure with $Pnam$ symmetry, and at $T_2 = 180$ K it transitions to the polar ground-state structure $P2_1am$ [21]. These phases differ in the stacking of the CO/OO along the c axis: denoting the two phases of the CO as α and β, there is $\alpha\alpha\beta\beta$ stacking in $Pnam$ and $\alpha\alpha$ stacking in $P2_1am$. Table I compares the structural properties of the $P2_1am$ ground state determined from experiment and obtained from DFT + U, which show satisfactory agreement.

Figure 2 depicts the experimentally determined electronic and magnetic ground state of $\mathrm{SmBaMn_2O_6}$. The CO typically is understood to arise from a disproportionation of the Mn into $\mathrm{Mn^{3+}}$ and $\mathrm{Mn^{4+}}$ sites, which form a checkerboard pattern in the ab plane, establishing two sublattices. The electronic configuration of $\mathrm{Mn^{3+}}$ is $t_{2g}^3 e_g^1$, so a Jahn-Teller instability yields a $d_{x^2-r^2}/d_{y^2-r^2}$ OO on the $\mathrm{Mn^{3+}}$ sublattice [3,26,27]. At $T_N = 260$ K, $\mathrm{SmBaMn_2O_6}$ develops CE-AFM order, which consists of zigzag chains of FM-coupled spins, where the $\mathrm{Mn^{3+}}$ ($\mathrm{Mn^{4+}}$) sites sit at the straight sections (corners). These chains are AFM coupled to each other within the ab plane and along c. Our calculations reproduce this coupled CO/OO/CE-AFM state. [28]

III. DECOMPOSITION OF THE GROUND-STATE CRYSTAL STRUCTURE

Having confirmed that our computational parameters reproduce the salient features of the experimental ground state, we now analyze the ground-state crystal structure in detail. The $P2_1am$ structure is highly distorted with respect to the high-symmetry reference structure $P4/mmm$ shown in

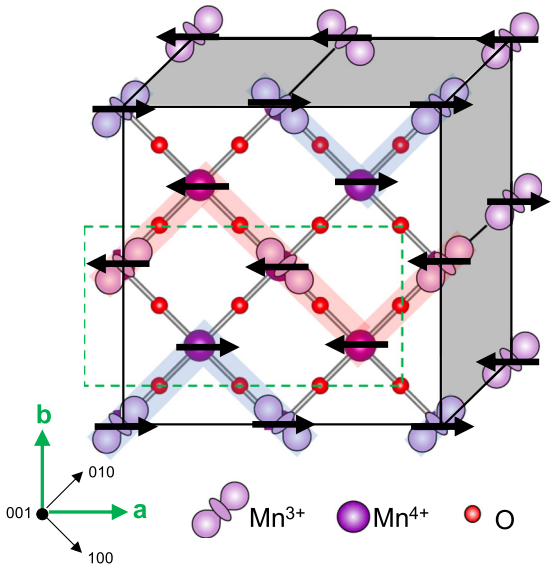

FIG. 2. Coupled ground-state charge, orbital, and spin order of $SmBaMn_2O_6$. The Mn^{3+}/Mn^{4+} CO forms a checkerboard in the *ab* plane. The Mn^{3+} sites host a $d_{x^2-r^2}/d_{y^2-r^2}$ OO, which form stripes parallel to the *b* axis. The spins order in a CE-type AFM pattern, where they form FM-coupled zigzags in the *ab* plane (indicated by light blue and red). These zigzags are AFM coupled to each other within the *ab* plane and also along *c*. The crystallographic unit cell is shown by the dashed green box, and the CE-AFM magnetic unit cell is shown by the black box. The green arrows indicate the setting of the orthorhombic axes *a* and *b* relative to the tetragonal axes.

Fig. 3(a). The $P2_1am$ structure decomposes into four distortions that transform like irreducible representations (irreps) of $P4/mmm$. These distortions, shown in Figs. 3(b)–3(e), are an out-of-phase ($a^-a^-c^0$ in Glazer notation [29]) octahedral tilting distortion that transforms like M_5^-, a breathing distortion coupled to the Mn^{3+}/Mn^{4+} CO that transforms like M_4^+, a polar distortion that transforms like Γ_5^-, and a distortion that transforms like Σ_2. Due to its low symmetry, the Σ_2 distortion encompasses a complex set of atomic displacements which form stripes parallel to the *b* axis; we refer to this as the "stripe distortion" in this work and describe it in more detail in a subsequent section. To assess the contributions of these four distortions to the ground-state structure, Table I reports the decomposition of the $P2_1am$ structure, both obtained from experiment (Ref. [21]) and from DFT + *U* structural relaxations, into symmetry-adapted modes of $P4/mmm$. The M_5^- octahedral tilt and the Σ_2 stripe distortion have large amplitudes, while the M_4^+ breathing and the Γ_5^- polar distortions make smaller contributions.

IV. FREE-ENERGY EXPANSION

To uncover how the structural distortions described above relate to each other, we perform a Landau free-energy expansion about the $P4/mmm$ reference structure. The lowest-order terms are

$$F_1 = \tfrac{1}{2}\alpha_t Q_T^2 + \tfrac{1}{4}\beta_t Q_T^4 + \tfrac{1}{2}\alpha_s\left(s_1^2+s_2^2\right) + \tfrac{1}{4}\beta_s\left(s_1^2+s_2^2\right)^2 + \tfrac{1}{2}\gamma_s s_1^2 s_2^2 + \tfrac{1}{2}\alpha_b Q_b^2 + \tfrac{1}{2}\alpha_p Q_P^2 + F_{tss} + F_{bss} + F_{tbp}, \quad (1)$$

where

$$F_{tss} = \delta_{tss} Q_T s_1 s_2, \quad (2)$$

$$F_{bss} = \delta_{bss} Q_b\left(s_1^2 - s_2^2\right), \quad (3)$$

and

$$F_{tbp} = \delta_{tbp} Q_T Q_b Q_P \quad (4)$$

are third-order coupling terms. Here, the order parameters Q_T, Q_b, and Q_P are the amplitudes of the M_5^- tilt, M_4^+ breathing, and Γ_5^- polar distortions, respectively. The Σ_2 stripe distortion is described by a two-dimensional order parameter (s_1, s_2), where s_1 and s_2 give the distortion amplitude on the two sublattices established by the CO/breathing distortion; the total amplitude is $Q_s = \sqrt{s_1^2 + s_2^2}$. For simplicity, Eqs. (1)–(4) are

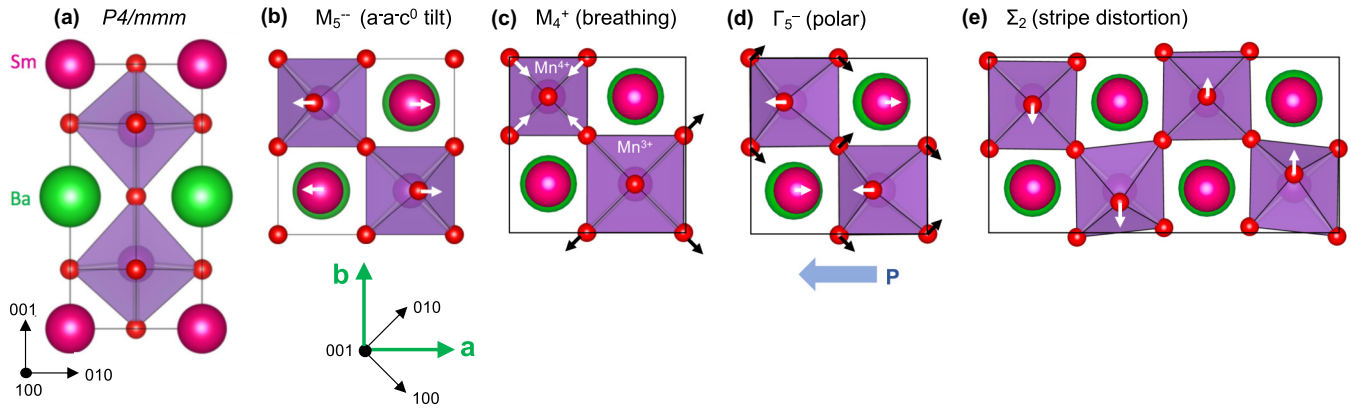

FIG. 3. Structural distortions that contribute to the ground-state crystal structure. (a) High-symmetry reference structure $P4/mmm$. The ground-state $P2_1am$ structure decomposes into four structural distortions that transform like irreps of $P4/mmm$: (b) an out-of-phase octahedral tilt that transforms like M_5^-, (c) a breathing distortion coupled to the Mn^{3+}/Mn^{4+} charge order that transforms like M_4^+, (d) a polar mode that transforms like Γ_5^-, and (e) a set of displacements that form in stripes along *b* and transform like Σ_2. In (c) and (d), the distortion amplitudes are artificially increased for better visualization. For clarity, in (e) only the apical oxygen displacements are highlighted with arrows, although all atoms displace from their high-symmetry positions. The green arrows indicate the setting of the orthorhombic axes *a* and *b* relative to the tetragonal axes.

TABLE II. Parameters from fitting the free-energy expansion in Eqs. (1)–(4) to the energy surfaces in Fig. 4. Since we calculate the energy surfaces along a fixed Σ_2 direction, we omit γ_s from Eq. (1).

α_t -0.31 eV/Å^2	β_t 0.55 eV/Å^4	δ_{tss} -0.47 eV/Å^3
α_s -0.05 eV/Å^2	β_s 0.73 eV/Å^4	δ_{bss} -1.48 eV/Å^3
α_b 2.80 eV/Å^2		δ_{tbp} -0.28 eV/Å^3
α_p 1.30 eV/Å^2		

restricted to one orthorhombic twin of $SmBaMn_2O_6$ (treating both twins requires higher-dimensional order parameters, as we discuss below).

Table II reports the coefficients of Eq. (1), obtained by freezing combinations of the M_5^-, M_4^+, Σ_2, and Γ_5^- distortions into $P4/mmm$ and fitting the resulting energy surfaces (Fig. 4). For these calculations, we impose A-AFM order and fix the lattice parameters to those of $P4/mmm$ relaxed with A-AFM order. The $P2_1am$ symmetry requires that $s_1 \neq s_2$; we fix the Σ_2 order-parameter direction to be (0.88, 0.47), that is, we freeze in amplitude Q_s where $s_1 = 0.88Q_s$ and $s_2 = 0.47Q_s$. This is the direction that occurs in the DFT + U-relaxed $P2_1am$ A-AFM state (see Appendices C and D for details). For clarity, throughout this work we distinguish between *variables* (s_1, s_2) which define an order-parameter space, *directions* (a, b) which are lines through the order-parameter space (amplitudes of a and b can vary), and *points* in the order-parameter space $(\tilde{s}_1, \tilde{s}_2)$ with fixed amplitude and direction.

We first freeze in each distortion individually [Fig. 4(a), left panel] and find that $P4/mmm$ is unstable to the M_5^- tilt, very weakly unstable to the Σ_2 stripe distortion, and stable with respect to the M_4^+ breathing distortion. This observation is significant because it means that the couplings in Eqs. (2) and (3) must induce the M_4^+ breathing distortion and the majority of the Σ_2 stripe distortion amplitude.

To make this clear, we compute energy surfaces where, in each calculation, we hold one of Q_T, Q_b, and Q_s to a fixed amplitude, and then freeze in one of the remaining two distortions [(Fig. 4(a), center panel]. The lower highlighted branch shows that once the unstable M_5^- tilt has condensed, Eq. (2) lowers the energy by inducing a portion of the Σ_2 stripe amplitude. The upper highlighted branches show that Eq. (3) strongly lowers the energy (notice the large negative value of δ_{bss} in Table II) by inducing Q_b and another portion of the Σ_2 stripe amplitude. The right panel of Fig. 4(a) shows energy surfaces obtained by fixing the amplitudes of two distortions and freezing in the final one [these again reflect the couplings in Eqs. (2) and (3)].

V. COUPLINGS BETWEEN THE STRUCTURAL, ELECTRONIC, AND MAGNETIC ORDER PARAMETERS

Our observation that F_{bss} induces the breathing distortion is significant because this underlies a direct link between the stripe distortion and the electronic and magnetic degrees of freedom in $SmBaMn_2O_6$. To make this clear, we include electronic and magnetic order parameters in our free-energy expansion. Since the electronic CO has the same symmetry as the breathing distortion, its order parameter Q_{CO} couples in the same way to the stripe distortion:

$$F_{cs} = \eta_{cs} Q_{CO}\left(s_1^2 - s_2^2\right). \tag{5}$$

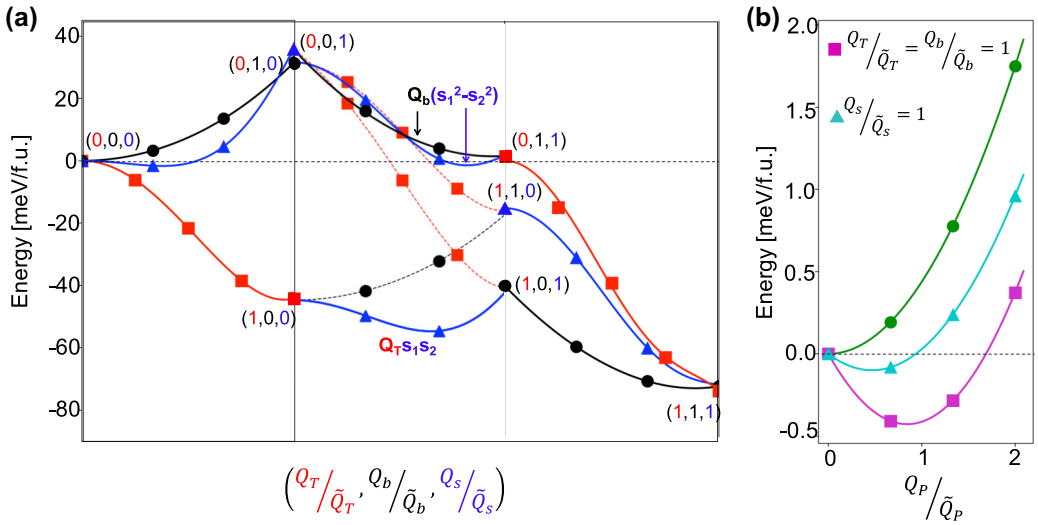

FIG. 4. Understanding how structural distortion couplings establish the ground state. The energy surface in the space defined by the M_5^-, M_4^+, and Σ_2 distortions is shown in (a). The triplet $(Q_T/\tilde{Q}_T, Q_b/\tilde{Q}_b, Q_s/\tilde{Q}_s)$ indicates the combination of M_5^-, M_4^+, and Σ_2 distortions frozen into $P4/mmm$ along a given branch. The color and symbol for each curve in each panel indicate the distortion amplitude that is changing along the curve, so only one distortion is changing along any curve in any panel. In the center panel, the curves discussed in the main text are shown with solid lines, and are labeled by the coupling terms that are active. Here, $\tilde{Q}$ are the distortion amplitudes obtained from the DFT + U-relaxed $P2_1am$ structure with A-AFM. The stripe distortion order parameter (s_1, s_2) is fixed along the (0.88, 0.47) direction, which is the direction obtained in the DFT + U-relaxed $P2_1am$ A-AFM state. (b) Shows energy surfaces obtained by freezing in the Γ_5^- distortion alone (green circles), with fixed $Q_s = \tilde{Q}_s$ (cyan triangles), and with fixed $Q_T = \tilde{Q}_T$ and $Q_b = \tilde{Q}_b$ (magenta squares). For all calculations, the lattice parameters are fixed to those of $P4/mmm$ with A-AFM order, and A-AFM order is imposed (see Appendix E for details).

TABLE III. Decomposition of the Σ_2 stripe distortion for both the experimental (Ref. [21]) and DFT+U-relaxed $P2_1am$ CE-AFM structures into physically intuitive displacements. The displacements have different amplitudes on the Mn^{3+} and Mn^{4+} sublattices, which are indicated by $\tilde{s}_{Mn^{3+}}$ and $\tilde{s}_{Mn^{4+}}$, respectively. The amplitudes are given in Å for the 40-atom unit cell.

Displacement type	$\tilde{s}_{Mn^{3+}}$ Expt.	$\tilde{s}_{Mn^{4+}}$ Expt.	$\tilde{s}_{Mn^{3+}}$ DFT	$\tilde{s}_{Mn^{4+}}$ DFT
Jahn-Teller (O_{eq})	0.18	0.02	0.24	0.02
$a^0a^0c^+$ (O_{eq})	0.34	0.04	0.46	0.06
$a^-a^-c^0$				
O_{ap} (Sm layer)	0.49	0.15	0.53	0.26
O_{ap} (Ba layer)	0.02	0.04	0.05	0.08
O_{eq}	0.22	0.14	0.28	0.21
Mn	0.12	0.01	0.20	0.00
Sm	0.01	0.03	0.05	0.07
Ba	0.07	0.00	0.13	0.01
Total	0.68	0.22	0.83	0.36

Therefore, *by symmetry*, the large-amplitude stripe distortion always accompanies the electronic CO, suggesting a far richer electron-lattice coupled state than is typically appreciated in CO models that focus on the electronic instabilities and associated small-amplitude breathing distortions alone. Intriguingly, recent experiments have revealed large-amplitude cation displacements accompanying CO in other manganites [30,31].

The CE-AFM also couples directly to the stripe distortion. Two magnetic order parameters define the CE-AFM state (one for each sublattice) [32,33]: $L_{CE} = (L_1, L_2)$ and $X_{CE} = (X_1, X_2)$, which describe the magnetic ordering on the Mn^{3+} and Mn^{4+} sublattices, respectively. The coupling between Q_{CO} and the CE-AFM order parameters is well known [33]:

$$F_{cL} = \eta_{cL} Q_{CO}\left(L_1^2 - L_2^2\right) + \eta_{cX} Q_{CO}(X_1^2 - X_2^2). \quad (6)$$

Combining Eqs. (5) and (6), the coupling between CE-AFM and the stripe distortion is

$$F_{sL} = \eta_{sL}\left(s_1^2 - s_2^2\right)(L_1^2 - L_2^2) + \eta_{sX}\left(s_1^2 - s_2^2\right)(X_1^2 - X_2^2). \quad (7)$$

Equations (5)–(7) show that the stripe distortion is a structural control knob to manipulate these electronic and magnetic orders, which we discuss more below.

To better understand this important structural distortion, Table III presents a physically intuitive decomposition of the stripe distortion into several types of atomic displacements [formally, these displacements are all symmetry-adapted modes that transform like Σ_2 (see Appendix D)]. Starting with the oxygen displacements, a relatively small component comes from the Jahn-Teller distortion associated with the $d_{x^2-r^2}/d_{y^2-r^2}$ OO on the Mn^{3+} sublattice. The remaining oxygen displacements can be viewed as $a^0a^0c^+$ octahedral rotationlike and $a^-a^-c^0$ octahedral tiltlike distortions on each sublattice that optimize Sm/Ba-O bonding. The apical oxygen displacements in the Sm layer, which relieve the severe underbonding of the Sm cations, makes by far the largest contribution to the stripe distortion amplitude. Finally, small displacements of the Sm, Ba, and Mn cations contribute the remaining amplitude.

VI. FERROELECTRIC MECHANISM

We now continue our energy surface analysis to elucidate the ferroelectric mechanism in $SmBaMn_2O_6$. Figure 4(b) shows that $P4/mmm$ is stable with respect to the Γ_5^- polar distortion, which means that a nonlinear coupling to other order parameters must induce the polarization. Recently, the concept of "hybrid improper ferroelectricity" has been introduced in other families of layered perovskite oxides, where a fixed symmetry-lowering mechanism (such as layering) removes a subset of symmetries, and then an active set of structural distortions breaks the remaining inversion symmetries and induces a polarization [34–36]. We find that ferroelectricity in $SmBaMn_2O_6$ arises from the same crystal chemical idea. First, the Sm/Ba ordering along c removes the inversion centers on the Mn sites. Then, condensation of the coupled M_5^-, M_4^+, and Σ_2 distortions breaks the remaining symmetries, establishing the $P2_1am$ space group and inducing the polarization.

All the couplings in Eqs. (2)–(4) are required to establish the polar state. In particular, the interplay of Eqs. (2) and (3) stabilizes the Σ_2 order-parameter *direction* that establishes the polar $P2_1am$ space group. To specify the symmetry of structures described by multidimensional order parameters, the direction in order-parameter space must be given. As shown in Table I, the $(a, b,0,0)$ direction of Σ_2 establishes $P2_1am$, where a and b are real numbers that are not equal to each other (see Appendix C). The Σ_2 order parameter is four dimensional, however, if we work within one orthorhombic twin as we are presently, then we can specify the direction as (a, b).

To see how the (a, b) direction is stabilized, note that Eq. (2) is nonzero only if both s_1 and s_2 are nonzero, and for a fixed amplitude Q_s, is maximal if $s_1 = s_2$. This term alone stabilizes the (a, a) direction of Σ_2. In contrast, Eq. (3) is nonzero only if $s_1 \neq s_2$, and for a fixed Q_s is maximal if $s_2 = 0$, stabilizing the $(a,0)$ direction of Σ_2. As a result, neither term by itself can establish the (a, b) direction of Σ_2, but when they act together this becomes the energetically preferable direction.

A consequence is that multiple coupling terms induce the polarization. The lowest-order such term is a trilinear coupling given in Eq. (4). We extend the free-energy expansion to higher order and find additional coupling terms linear in Q_P:

$$F_2 = \zeta_{pts} Q_P Q_T \left(s_1^2 - s_2^2\right) + \zeta_{pbs} Q_P Q_b s_1 s_2 + \zeta_{pss} Q_P s_1 s_2 \left(s_1^2 - s_2^2\right). \quad (8)$$

Figure 4(b) shows how multiple coupling terms contribute to inducing the polarization. First, holding Q_T and Q_b at fixed amplitude, we freeze in Q_P (magenta squares), and find that the energy surface minimum shifts to finite amplitude. This shows that the trilinear coupling in Eq. (4) induces Q_P. Next, holding Q_s fixed and again freezing in Q_P (cyan triangles), the minimum again shifts to a smaller (but nonzero) amplitude. This shift is smaller because this energy surface reflects the last term in Eq. (8), which is at fifth order. Freezing in

different distortion combinations and performing analogous calculations shows the contributions of the other terms in Eq. (8).

Since the M_5^-, M_4^+, and Σ_2 distortions act together to establish the polar state, $SmBaMn_2O_6$ has a hybrid improper ferroelectric mechanism. Previous work described $SmBaMn_2O_6$ as an improper ferroelectric [22], which does not take into account the combined action of Q_T and Q_b in establishing the (a, b) direction of Σ_2.

VII. COMPETING PHASES

Our symmetry-based approach provides a natural framework with which to systematically investigate phases that may compete with the bulk ground state of $SmBaMn_2O_6$. First, we identify metastable structural phases by exploring the energy landscape in the space defined by the M_5^- and the Σ_2 distortions since these distortions have the largest amplitudes in the ground-state structure. Formally, this means that we enumerate all isotropy subgroups generated by distinct directions of the M_5^- and Σ_2 irreps. Then, we use DFT + U to investigate the structural, electronic, and magnetic properties of $SmBaMn_2O_6$ when the symmetry is constrained to each of these space groups. We explore all phases with both FM and A-AFM orders imposed since both occur in the bulk $R BaMn_2O_6$ experimental phase diagram. These magnetic orders compete with Q_b and the stripe distortion (if $s_1 \neq s_2$) via biquadratic couplings:

$$\begin{aligned} F_{Mb} &= \eta_{Mb} Q_b^2 M^2 + \eta_{Ab} Q_b^2 L_A^2 \\ F_{Ms} &= \eta_{Ms}\left(s_1^2 - s_2^2\right) M^2 + \eta_{As}\left(s_1^2 - s_2\right)^2 L_A^2 \end{aligned} \tag{9}$$

where M and L_A are the FM and A-AFM order parameters, respectively.

We start with the two-dimensional M_5^- order parameter, which has three symmetry-distinct directions: $(a,0)$, (a, a), and (a, b). These define space groups *Pmam*, *Cmmm*, and $P2/m$, respectively. The $(a,0)$ direction of M_5^- is found in the ground-state structure, while the (a, a) direction gives the experimentally observed high-temperature phase (*Cmmm*) [21]. The difference between these phases is the octahedral tilt axis: the octahedra tilt about the tetragonal [110] axis in *Pmam*, and about [100] in *Cmmm*. We next perform DFT + U structural relaxations with the symmetry constrained to *Pmam* and *Cmmm* and separately impose both FM and A-AFM orders; the resulting total energies are shown in Table IV. For both magnetic configurations, the *Cmmm* structure is lower energy than *Pmam*. In fact, the *Cmmm* FM phase is only 10.8 meV/f.u. higher in energy than the $P2_1am$ CE-AFM ground state.

There are many distinct directions and corresponding isotropy subgroups of the Σ_2 order parameter since it is four dimensional. Table IV reports the total energies obtained from structural relaxations with the symmetry constrained to several of these subgroups [28]. Most directions of Σ_2, such as the $(a,0,0,0)$ direction shown in Table IV, only slightly lower the energy relative to the high-symmetry reference $P4/mmm$. The lowest-energy structural phase above the ground state is *Pbam*, established by the $(a, a,0,0)$ direction of Σ_2. $P2_1am$ with A-AFM order is only 4.4 meV/f.u. higher energy than with CE-AFM order (with FM order, it relaxes to the higher-symmetry *Pbam*). The competing phases are all centrosymmetric and metallic with the exception of the $P2_1am$ A-AFM phase, which has a small insulating gap [28]. In the next sections, we discuss how these competing phases may stabilize in $SmBaMn_2O_6$.

TABLE IV. Isotropy subgroups established by selected distinct directions of the M_5^- and Σ_2 irreps. Energies are obtained from DFT+U structural relaxations with the symmetry constrained to each space group and FM or A-AFM order imposed, and are given in meV per formula unit (f.u.). The right two columns report the ratio of the lattice parameters c and a (c/a), where $c/a = 2$ corresponds to zero tetragonal distortion (for orthorhombic space groups, we average the a and b axes to compute these ratios).

M_5^-	Σ_2	Space group	Energy FM	Energy A-AFM	c/a FM	c/a A-AFM
		$P4/mmm$	85.25	94.52	1.99	1.94
$(a,0)$		*Pmam*	39.57	46.09	1.98	1.93
(a, a)		*Cmmm*	10.80	16.11	1.97	1.93
	$(a,0,0,0)$	*Pmam*	83.50	74.64	1.99	1.94
$(0,a)$	$(a, a,0,0)$	*Pbam*	29.13	18.52	1.97	1.93
$(0,-a)$	$(a, b,0,0)$	$P2_1am$		4.39		1.93
				CE-AFM		CE-AFM
$(0,-a)$	$(a, b,0,0)$	$P2_1am$		0.0		1.93

VIII. COUPLED STRUCTURAL DOMAINS AND DOMAIN WALLS

This section shows that the domain structure of $SmBaMn_2O_6$ encodes the coupling and competition of order parameters analyzed in previous sections. We first organize the bulk domains, and then explore the domain walls.

The $P2_1am$ ground state has 16 structural domains established by the different settings of the $(a, b,0,0)$ direction of Σ_2 (listed in Appendix F). These domains are divided between two orthorhombic twins. The eight domains within one twin are represented as points in the two-dimensional order-parameter space (s_1, s_2) that defines the Σ_2 distortion in that twin [Fig. 5(a)]. Once the Σ_2 order parameter is chosen for a given domain, the couplings in Eqs. (2)–(4) determine the signs of the other structural order parameters in that domain. The domains in each quadrant of Fig. 5(a) have the same octahedral tilt ($\pm Q_T$), the domains in the pink (blue) regions have the same CO/breathing distortion Q_b ($-Q_b$), and the domains in the hatched (solid) regions have the same polarization Q_P ($-Q_P$). Thus, these structural domains directly visualize the couplings between structural distortions.

There are several distinct types of domain walls that separate the domains in Fig. 5(a). Within order-parameter space, domain walls are represented as paths between the domains. These paths can be thought of as a generalization of intrinsic ferroelectric switching paths, which connect domains with different polarization directions, to other domain types [37]. To enumerate the different domain walls in $SmBaMn_2O_6$, we consider all paths that connect the (a, b) domain to the other domains [thick gray lines in Fig. 5(b)]. The crystal structure evolves along each path, and the highest-energy structure

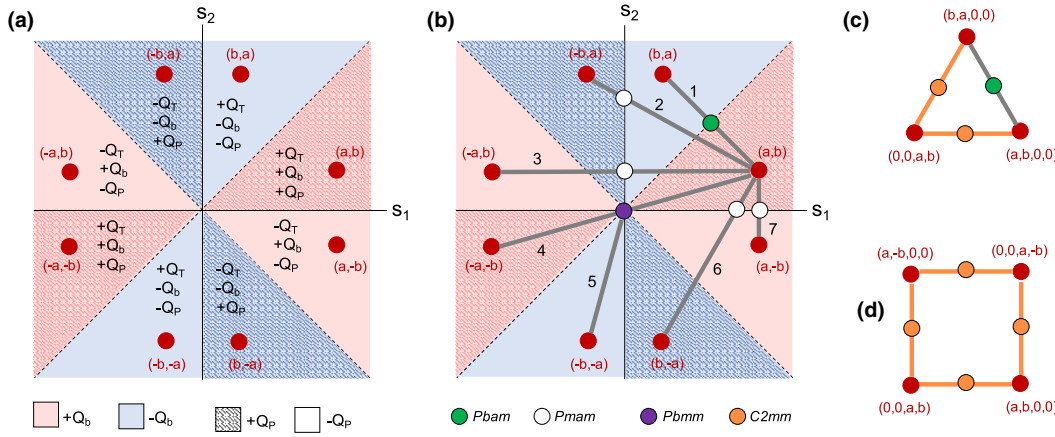

FIG. 5. Visualizing coupled structural domains and revealing competing phases. (a) Structural domains within one orthorhombic twin of $SmBaMn_2O_6$. The domains (red dots) are points within the two-dimensional space defined by the Σ_2 stripe order-parameter directions (s_1, s_2) for that twin. The domains in the top right and lower left quadrants have octahedral tilt Q_T, while the domains in the other two quadrants have tilt $-Q_T$. The pink (blue) regions denote regions with CO/breathing distortion $+Q_b$ $(-Q_b)$, and the hatched (solid) regions indicate regions with polarization Q_P $(-Q_P)$. (b) Paths between domains, indicated by gray lines, with the barrier structures labeled by colored circles: *Pbam* (green), *Pmam* (white), and *Pbmm* (purple). Extending to the four-dimensional order-parameter space defined by the full Σ_2 order parameter (s_1, s_2, s_3, s_4), we can construct closed paths that represent (c) threefold and (d) fourfold domain wall vortices. Here, the thick orange lines indicate paths between domains in opposite orthorhombic twins (twin walls), the orange circle is the *C*2*mm* barrier for this path.

gives the energy barrier for that path. Since $SmBaMn_2O_6$ is described by several multidimensional order parameters, there can be more than one type of path between a given pair of domains (in the language of ferroelectric switching, these are one-step versus two-step paths). These paths pass through different sequences of structures and have different energy barriers. While paths through order-parameter space cannot provide quantitative information on domain wall properties (because they rely on bulk calculations), they provide an efficient strategy to organize the many domain wall types.

All paths in Fig. 5(b) connect different Σ_2 domains, so they all describe stripe distortion domain walls. Paths that cross the s_1 and s_2 axes also are octahedral tilt antiphase walls, paths that connect domains in blue and pink regions are CO/breathing domain walls, and paths that connect domains in hatched and solid regions are 180° polar walls. For example, path 1 in Fig. 5(b) describes a CO and polar domain wall. The barrier structure for this path is *Pbam*. Paths 2, 3, 6, and 7 all describe octahedral tilt antiphase walls and have barrier structure *Pmam* [the $(a,0,0,0)$ direction of Σ_2]. Paths 2 and 6 (3 and 7) also are CO (polar) walls. Along paths 4 and 5, both s_1 and s_2 reverse sign, so the barrier structure is *Pbmm* [the $(0,a)$ direction of M_5^-]. These barrier structures are the competing phases discussed above, so Table IV reports their energies. While the exact barrier energy depends on the magnetic state, irrespective of the magnetic states in Table IV, the energy ordering from lowest to highest is *Pbam* (path 1), *Pbmm* (paths 4 and 5), *Pmam* (paths 2, 3, 6, 7). This ordering reflects that turning off the small-amplitude Q_b (path 1) costs less energy than turning off the large-amplitude octahedral tilt Q_T (paths 2, 3, 6, 7).

In addition to the paths in Fig. 5(b) that all stay within one orthorhombic twin, there are paths that connect domains in opposite twins (twin walls). Describing these paths requires the four-dimensional Σ_2 order parameter (s_1, s_2, s_3, s_4); s_1 and s_2 are nonzero in one twin, and s_3 and s_4 are nonzero in the other (see Appendix D). As an example, we consider the path between the $(a, b,0,0)$ and $(0,0,a, b)$ domains. The barrier structure along this path is the (a, b, a, b) direction of Σ_2, with symmetry *C*2*mm* (all paths between domains in opposite twins have the same *C*2*mm* barrier). The *C*2*mm* structure relaxes to *Cmmm* (listed in Table IV) after DFT + U structural relaxations, which has much lower energy than the barriers for the paths in Fig. 5(b).

IX. DOMAIN WALL VORTICES AND ANTIVORTICES

The observation that the *Cmmm* barrier is much lower than the other barriers has significant implications for the stability of the different domain wall types. The paths in Fig. 5(b) are one-step paths, which means that they pass directly from one domain to the other via one barrier structure. An alternative is a two-step path, where the path passes through a domain in the other orthorhombic twin. For example, the two-step alternative to path 3 in Fig. 5(b) is $(a, b,0,0) \rightarrow (0,0,a, b) \rightarrow (-a, b,0,0)$. The barrier for the first and second steps of this path are the (a, b, a, b) and $(-a, b, a, b)$ directions of Σ_2, respectively, which are just different *C*2*mm* domains (which relax to *Cmmm*). Therefore, for every path in Fig. 5(b), there is an alternative two-step path with barrier *Cmmm*. For a given pair of domains, comparing the one-step barrier to twice the two-step barrier indicates the lowest-energy path. To make this comparison, for each structure we choose the lowest-energy magnetic state from Table IV, so the barrier energies (in meV/f.u.) are 10.8 (*Cmmm*), 18.5 (*Pbam*), 39.6 (*Pbmm*), and 74.6 (*Pmam*). This implies that path 1 is the only one-step path that is lower energy than the two-step alternative, so it is energetically favorable for all other paths in Fig. 5(b) to decay into the two-step path (pairs of twin walls). This does not depend on our particular choice of the barrier magnetic state, for example, choosing the barriers to be all A-AFM or all FM leads to the same conclusion.

Structural domain walls terminate at the edge of the sample or they merge with other walls at domain wall vortices which appear a range of complex materials [6]. Within order parameter space, closed paths that start and end at the same domain and are traversed (counter)clockwise represent domain wall (anti)vortices. The number of domains that a closed path passes through gives the order of the vortex. Figures 5(c) and 5(d) show the domain wall vortices that we find to be energetically favorable in $SmBaMn_2O_6$. Two types of walls are stable against decaying into lower-energy walls: path 1 in Fig. 5(b) (CO/polar wall, barrier *Pbam*) and the path between orthorhombic twins (barrier *Cmmm*). Starting at the $(a, b,0,0)$ domain, we construct a closed path $(a, b, 0, 0) \rightarrow (b, a,0,0) \rightarrow (0,0,a, b) \rightarrow (a, b,0,0)$, shown in Fig. 5(c). This path describes a threefold vortex where one CO/polar wall and two twin walls merge. We also can construct an alternative closed path $(a, b, 0, 0) \rightarrow (0,0,a, -b) \rightarrow (a, -b,0,0) \rightarrow (0,0,a, b) \rightarrow (a, b,0,0)$ shown in Fig. 5(d), which describes a fourfold vortex where four twin walls meet. This indicates that a domain pattern characterized by a network of threefold and fourfold domain wall vortices is energetically favorable in $SmBaMn_2O_6$. A threefold/fourfold vortex domain structure has been observed in $Pr(Sr_{1-x}Ca_x)_2Mn_2O_7$ [6,11].

X. SCENARIOS FOR ELECTRONIC AND MAGNETIC DOMAIN WALL STATES

Since domain walls locally modulate the crystal structure, they can reveal competing phases that are not present in the bulk domains. Here, we speculate about electronic and magnetic states that may stabilize at $SmBaMn_2O_6$ domain walls. The barrier structures discussed above all host metallic FM or A-AFM states, so if the domain walls are sufficiently wide to realize a bulklike structure in the middle, these states may naturally stabilize. Furthermore, an implication of the coupling between the stripe distortion and CE-AFM [Eq. (7)] is that all structural walls [with the exception of path 7 in Fig. 5(b)] are also CE-AFM magnetic walls. The interruption of the CE-AFM order at the walls also may allow competing FM and A-AFM states to arise. Interestingly, recent work on manganite strips found that FM metallic edge states form at the edges of the strips, where the CE-AFM order is interrupted [38,39]. While mechanical boundary conditions and local structural relaxations not considered here influence domain wall states, these scenarios show how the naturally occurring structural modulation at domain walls may stabilize competing phases.

XI. PHASE CONTROL WITH EPITAXIAL STRAIN

As a second example of how structural modulation can control the electronic/magnetic state, we investigate how epitaxial strain impacts single-domain $SmBaMn_2O_6$ thin films. Comparing the c/a ratio for the *bulk* ground state and competing phases in Table IV, we find that regardless of the structural symmetry, $c/a \approx 1.98$ with FM order and $c/a \approx 1.93$ for CE- and A-AFM orders. Thus, c/a provides a knob to tune between FM and AFM states. The application of epitaxial strain in thin films is a well-known way to control c/a: compressive strain applied in the ab plane shortens a and b while c lengthens to maintain an approximately constant volume. This is different from chemical substitution, where all lattice parameters change at approximately the same rate (Appendix G).

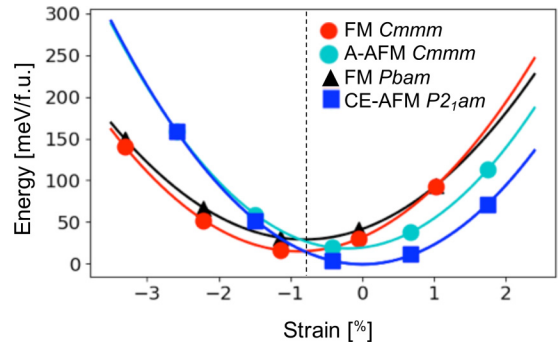

FIG. 6. Phase control with epitaxial strain. Total energy versus strain for several structural and magnetic phases of $SmBaMn_2O_6$. The 0% strain is defined relative to the CE-AFM lattice constants. The dashed line indicates the strain value at which the energy of the CE-AFM $P2_1am$ and FM *Cmmm* phases are energetically degenerate. Negative and positive strain values correspond to compressive and tensile strains, respectively.

Figure 6 shows the total energy of several structural and magnetic phases of $SmBaMn_2O_6$ as a function of epitaxial strain. For tensile and small compressive strains, the polar $P2_1am$ CE-AFM phase is the lowest energy, while at larger compressive strains, the *Cmmm* FM state becomes the lowest. At 0.8% compressive strain, these two phases are energetically degenerate and thus compete for the ground state. Assuming that the film hosts a mixture of these two states, this phase competition could enable cross-coupled control of magnetization and polarization: the application of a magnetic field would grow the *Cmmm* FM regions and shrink the $P2_1am$ polar regions, so that the magnetization (polarization) increases (decreases). Conversely, the application of an electric field may increase the polar regions and decrease the FM regions, so that the polarization (magnetization) increases (decreases). While this is a compelling idea, it is important to note that an applied electric field may instead promote the FM metallic phase in order to screen the field. Experiments on $Pr_{0.7}Ca_{0.3}MnO_3$ have revealed that an electric field of $\approx$7 kV/cm drives an insulator-metal transition [40,41]. Coercive fields of various types of ferroelectrics are in the 10–100 kV/cm range, although the field required to change the polarization magnitude (expand the polar regions) rather than completely flip the polarization would be lower. The outcome of electric field application on $SmBaMn_2O_6$ would depend on the balance of energy scales of polar domain wall motion and the insulator-metal transition.

To understand how strain impacts the barrier for magnetic field control, we consider a $P2_1am$ CE-AFM domain, and imagine applying a magnetic field that is perpendicular to the spin axis as shown in Fig. 7. This magnetic field rotates the spins so that they transform to a FM configuration. To describe this transformation, we select a reference spin and define θ to be the angle that this reference spin makes with the initial spin axis (so $\theta = 0^\circ$ is CE-AFM, $\theta = 90^\circ$ is FM). Then, for several intermediate θ we perform constrained spin

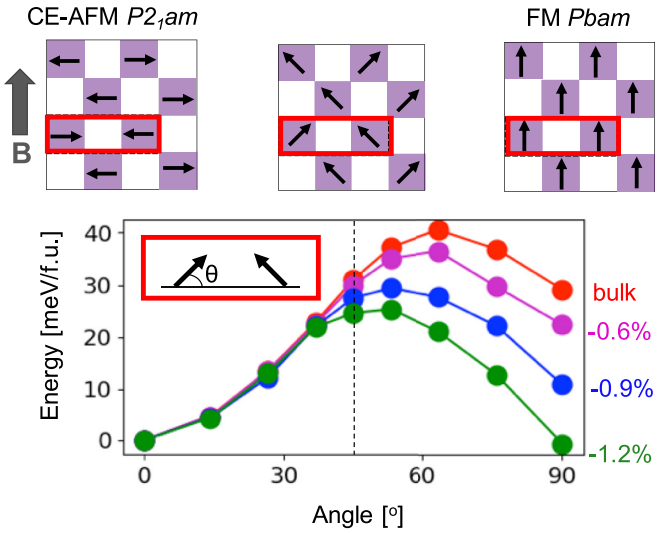

FIG. 7. Energy barrier between competing phases. Total energy versus constrained spin angle for bulk and compressively strained $SmBaMn_2O_6$. The angle that the left reference spin (in the red box) makes with the horizontal axis defines the spin angle θ, so $\theta = 0^\circ$ and 90° correspond to CE-AFM and FM, respectively. The dark gray arrow indicates the direction of the hypothetical magnetic field.

calculations, allowing the structure to fully relax at each θ. Since we start with $P2_1am$ and relax the structure at each step, the resulting FM phase at $\theta = 90^\circ$ has $Pbam$ symmetry, rather than the lower energy $Cmmm$ (so the barriers in Fig. 7 are an upper limit). As the compressive strain increases, the energy barrier between the $P2_1am$ CE-AFM and $Pbam$ FM phases decreases, which suggests that strain lowers the field strength needed to control the competing phases.

XII. DISCUSSION

We have shown how the interplay of several structural distortions underlies the coupled structural, electronic, and magnetic ground state of $SmBaMn_2O_6$. The coupled distortions induce the CO and an electrical polarization via a hybrid improper ferroelectric mechanism. Our approach allows a systematic exploration of metastable structures, from which we identify several low-energy FM and A-AFM centrosymmetric metallic phases that compete with the polar-insulating CO/OO/CE-AFM ground state. We show that the domain structure of $SmBaMn_2O_6$ visualizes the coupling and competition between these order parameters, via a set of coupled domains connected by threefold and fourfold domain wall vortices and antivortices. To assess this domain structure, we suggest microwave impedance microscopy, which already has been reported for the related compound $Pr(Sr_{1-x}Ca_x)_2Mn_2O_7$ [11].

In addition, we consider two examples where control of the complex $SmBaMn_2O_6$ crystal structure provides a knob to manipulate the electronic and magnetic states: at structural domain walls (which are a naturally occurring form of structural modulation in bulk systems), and in epitaxial thin films. In the latter example, we show how it is possible to tune $SmBaMn_2O_6$ to a regime where a centrosymmetric FM metallic state is energetically degenerate with the polar-insulating bulk ground state, which may enable cross-coupled control of polar and magnetic states.

Finally, we comment on the applicability of our results to other rare-earth manganites. While we focus here on the special case of A-site ordered $SmBaMn_2O_6$, the structural distortions as well as the CO/OO/CE-AFM, FM, and A-AFM phases that we investigate occur in many other manganites. In particular, we anticipate that the stripe distortion explored in detail here to be relevant more broadly for half-doped manganites (including A-site disordered materials). For example, experiments have reported that A-site disordered $La_{0.5}Ca_{0.5}MnO_3$ [42,43] and $Tb_{0.5}Ca_{0.5}MnO_3$ [44] in the CO/OO/CE-AFM phase have symmetry $P2_1/m$. Decomposing the experimental $La_{0.5}Ca_{0.5}MnO_3$ $P2_1/m$ structure from Ref. [43] with respect to cubic $Pm\bar{3}m$ (the reference structure for A-site disordered systems) reveals the presence of a large-amplitude stripe distortion in this material. We hypothesize that the link between CO and the stripe distortion that we identify in $SmBaMn_2O_6$ holds generally for half-doped manganites. We also expect that the coupling between CE-AFM and structural domains, the scenarios for FM and A-AFM domain wall states, and the tunability of the ground state between CE-AFM and FM states with epitaxial strain to be applicable for both A-site ordered and disordered half-doped manganites.

In contrast, other results depend on the A-site ordered structure. For example, A-site ordering is required to establish the polar crystal structure of $SmBaMn_2O_6$. In addition, we expect that the domain structure of A-site disordered half-doped manganites to be different from the threefold and fourfold domain wall vortex structure of A-site ordered $SmBaMn_2O_6$ discussed here. This is because A-site ordering reduces the structural order-parameter dimensions by establishing a preferential axis in the high-symmetry reference structure. For example, with A-site ordering the octahedral tilt and stripe distortion order parameters are two and four dimensional, respectively (as discussed above), while with A-site disordering, these order parameters are three and twelve dimensional, respectively. As a result, the A-site disordered manganites have a larger number of structural domains and more possible paths between domains (domain wall types) than the A-site ordered manganites. This would result in a complex domain structure which could be analyzed using the approach presented in this work.

ACKNOWLEDGMENTS

We acknowledge support from the U. S. Department of Energy, Office of Basic Energy Sciences, Materials Sciences and Engineering Division, under Award No. DE-SC0002334 and from the Army Research Office under grant W911NF-10-1-0345. E.A.N. also acknowledges support from the New Jersey Institute of Technology. This research used computational resources supported by the Cornell University Center for Advanced Computing and by Academic and Research Computing Systems at the New Jersey Institute of Technology.

E.A.N. and J.H. contributed equally to this work.

APPENDIX A: COMPUTATIONAL DETAILS

We perform density functional theory calculations using VASP [45,46] with the PBEsol exchange-correlation functional

TABLE V. Experimentally reported crystal and magnetic structures for $R\mathrm{BaMn_2O_6}$ compounds.

R	Temperature (K)	Space group	Magnetic order	Reference
Sm	400	$Cmmm$		[21]
Sm	300	$Pnam$		[21]
Sm	150	$P2_1am$	CE-AFM	[21]
Nd		$P4/mmm$	A-AFM	[16]
Nd	290	$P2_1am$		[51]
Pr		$P4/mmm$	A-AFM/CE-AFM coexistence	[16]
La		$P4/mmm$	FM/CE-AFM coexistence	[16]

[47]. We use a plane-wave basis with an energy cutoff of 500 eV. We treat the Mn onsite Coulomb interaction using the Liechtenstein formulation of the DFT + U method [48]. We set $U = 4.0$ eV and $J = 1.2$ eV; these values are chosen because they reproduce the bulk $R\mathrm{BaMn_2O_6}$ phase diagram (see Appendix B). The unit cell in the $P2_1am$ CE-AFM ground-state phase is $2\sqrt{2}a_0 \times 2\sqrt{2}a_0 \times 2c_0$, which contains 80 atoms. We use a $4 \times 4 \times 6$ Γ-centered k-point grid to sample Brillouin zone of the $P2_1am$ CE-AFM phase. For other structures and magnetic orders, we used smaller computational cells for some calculations where we chose the same density of k points that was used for the 80-atom cell. We used a force convergence tolerance of 10 meV/Å. Biaxial strain was applied by fixing the in-plane lattice constants a and b to a square and relaxing the out-of-plane lattice constant c and all atomic positions. For group-theoretical analysis we utilized the ISOTROPY software suite [49]. We visualized crystal structures using VESTA [50].

APPENDIX B: CHOICE OF U AND J PARAMETERS

Table V summarizes the experimentally reported $R\mathrm{BaMn_2O_6}$ phase diagram, also shown in Fig. 1. The ground state evolves from an AFM CO/OO polar insulator for $R = $ Sm, to a A-AFM metal for $R = $ Nd and Pr, to a FM metal for $R = $ La. However, note that as indicated in Table V, the experimental picture of the ground state for some systems remains unclear. To guide our choice of U and J parameters in the main text, we explore the bulk structural energetics as we vary these parameters for $R = $ Sm, Nd, and La (Fig. 8). First, fixing $J = 1.2$ eV and varying U, we find that for all three compounds [Figs. 8(a), 8(c), and 8(d)], the A-AFM state is stabilized for $U = 3$ eV, where the structure has symmetry $Cmmm$ for $R = $ Sm and Nd and $P4/mmm$ for $R = $ La. As U increases, the FM state becomes lower energy than the A-AFM state for all three compounds, however, for $R = $ Sm and Nd the CE-AFM state stabilizes more quickly and becomes the ground state for $U = 4$ eV. Based on these results, we select $U = 4.0$ eV to use in all other calculations within this work. In Fig. 8(b), we vary J for $\mathrm{SmBaMn_2O_6}$ (with U fixed to 4 eV). For small J, the $Cmmm$ FM phase is lowest energy, and then the $P2_1am$ CE-AFM phase stabilizes with increasing J. Based on this result, we choose $J = 1.2$ for all calculations. Note that this set of parameters reproduces the CO/OO CE-AFM ground state for $R = $ Sm and the $P4/mmm$ FM metallic ground state for $R = $ La. This set of parameters also predicts the CO/OO CE-AFM insulating state for $R = $ Nd, however, we note that as shown in Table V, there are conflicting reports of the ground state for this system.

APPENDIX C: ORDER-PARAMETER NOTATION

With the exception of the M_4^+ breathing distortion, the other structural distortions in $\mathrm{SmBaMn_2O_6}$ are described by multidimensional order parameters (the M_5^- tilt and Γ_5^- polar order parameters are two dimensional, and the Σ_2 order parameter is four dimensional). In analyzing these multidimensional order parameters, it is important to distinguish between the *amplitude* of the order parameter and its *direction* within the order-parameter space. This section describes our notation for these quantities.

For concreteness, here we consider the two-dimensional M_5^- tilt order parameter (T_1, T_2). The variables T_1 and T_2 define the two-dimensional order-parameter space, and at any particular point in this space the order-parameter amplitude is $Q_T = \sqrt{T_1^2 + T_2^2}$. To define the order-parameter directions, we use a and b to denote the order-parameter components T_i, where a and b are arbitrary numbers that are not equal to each other. Using this notation, the three distinct directions of the order parameter are $(T_1, T_2) = (a,0)$, (a, a), and (a, b). The key point is that each of these distinct directions defines a family of structures of a particular symmetry (with the order-parameter amplitude still a variable). The order-parameter amplitude $\tilde{Q}$ that minimizes the total energy for a particular structural symmetry can be obtained by performing DFT

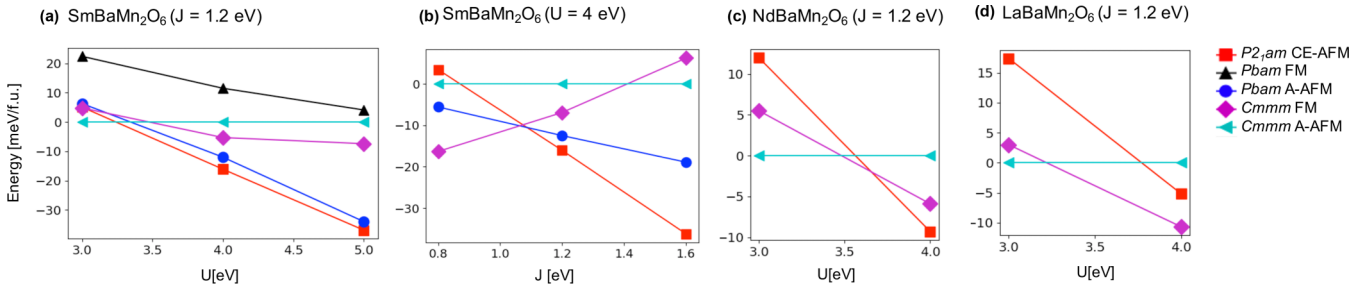

FIG. 8. Total energy of $\mathrm{SmBaMn_2O_6}$ as a function of (a) U (with fixed $J = 1.2$ eV), and (b) J (with fixed $U = 4$ eV). Total energy as a function of U for (c) $\mathrm{NdBaMn_2O_6}$ and (d) $\mathrm{LaBaMn_2O_6}$. For (c) and (d), $J = 1.2$ eV. All energies are referenced to the $Cmmm$ A-AFM energy.

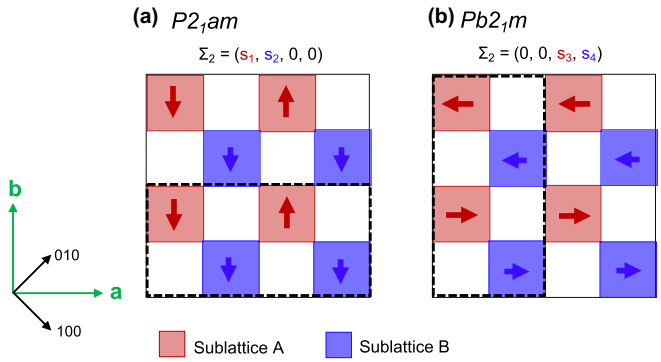

FIG. 9. Relationship between sublattices, the stripe distortion, and orthorhombic twins. Here, red and blue represent sublattices A and B, respectively. The red (blue) arrows represent the apical oxygen displacements on sublattice A (B), all other displacements that contribute to the stripe distortion are suppressed for clarity. With the setting of the orthorhombic axes a and b relative to the tetragonal axes shown, the two orthorhombic twins can be distinguished via different settings of the space group (a) $P2_1am$ and (b) $Pb2_1m$. The distortion forms stripes of upward and downward displacements perpendicular to the long axis, so in twin $P2_1am$ the stripes lie along b and in twin $Pb2_1m$ they lie along a. The black dashed line indicates the crystallographic unit cell.

structural relaxations constrained to that symmetry. Finally, for a given structural symmetry (defined by *distinct* direction of the order parameter) the structural domains are defined by the multiple order-parameter directions that are consistent with that symmetry. For example, the *Pmam* structure, defined by the (a,0) distinct direction, has four domains, labeled by the order-parameter directions (a,0), ($-a$,0), (0,a), and (0,$-a$).

Similarly, the Γ_5^- order parameter defines a two-dimensional order-parameter space (P_1, P_2), and the Σ_2 order parameter defines a four-dimensional space (s_1, s_2, s_3, s_4). In the analysis of the domain structure and switching paths in the main text, we label the domains of the $P2_1am$ ground state by the directions of the Σ_2 order parameter, for example, (s_1, s_2, s_3, s_4) = (a, b,0,0), (a, $-b$,0,0), etc. It is important to keep in mind that a and b are arbitrary numbers (with the symmetry constraint that they are unequal), the particular distortion amplitudes realized in the ground-state structure ($\tilde{s}_1$, $\tilde{s}_2$) are obtained from structural relaxations. We also label the barrier structures by the Σ_2 order-parameter direction that defines their symmetry (where again, the order-parameter amplitudes at the barrier are obtained by structural relaxations with the symmetry constrained to that of the barrier).

APPENDIX D: STRIPE DISTORTION

The Σ_2 stripe distortion is most naturally understood by dividing the MnO_2 plane into two sublattices (the same checkerboard sublattices as defined by the CO). Since in principle one can think about sublattices without CO, we call these sublattices A and B in the following discussion for generality. The relationship between these sublattices, the stripe distortion, and the orthorhombic twins is shown in Fig. 9.

Once the setting of the orthorhombic axes a and b is defined relative to the tetragonal axes as shown in Fig. 9, the two orthorhombic twins are labeled by different space-group settings, $P2_1am$ and $Pb2_1m$, shown in Figs. 9(a) and 9(b), respectively. The first two components of the four-dimensional Σ_2 order parameter (s_1 and s_2) give the stripe distortion amplitude for the domains in the $P2_1am$ orthorhombic twin ($s_3 = s_4 = 0$). Here, s_1 gives the distortion amplitude on sublattice A, and s_2 gives the distortion amplitude on sublattice B; the apical oxygen displacements on the two sublattices are indicated by red (blue) arrows (the rest of the displacements that contribute to the stripe distortion are suppressed for clarity). The last two components of the Σ_2 order parameter (s_3 and s_4) give the distortion amplitude for the domains in the $Pb2_1m$ orthorhombic twin ($s_1 = s_2 = 0$), with s_3 (s_4) giving the amplitude on sublattice A (B). In the $P2_1am$ twin, there are stripes of upward and downward displacements parallel to the b axis, while in the $Pb2_1m$ twin, the stripes lie along a. Finally, if one only considers domains within one orthorhombic twin, the Σ_2 order parameter can be treated as a two-dimensional quantity (s_1, s_2) as is done in the first part of the main text for simplicity.

Dividing the complex set of atomic displacements that contribute to the stripe distortion into physically intuitive groups helps us organize our thinking about this distortion. These physically intuitive displacements are shown in Figs. 10(a)–10(c) on sublattice A and in Figs. 10(d)–10(f) on sublattice B. Separate panels show the different displacements: the $a^-a^-c^0$ octahedral tiltlike distortion and cation displacements [Figs. 10(a) and 10(d)], the $a^0a^0c^+$ octahedral rotationlike distortion [Figs. 10(b) and 10(e)] and the Jahn-Teller distortion [Figs. 10(c) and 10(f)]. If displacements are only allowed on one sublattice at a time as in Figs. 10(a)–10(c) and 10(d)–10(f), the symmetry of the structure is *Pmam*, defined by the (a,0,0,0) direction of Σ_2 [note that this is a distinct structure from the *Pmam* defined by the (a,0) direction of M_5^-]. If displacements are allowed on both sublattices, but have equal amplitude ($s_1 = s_2$) the symmetry is *Pbam* [shown in Figs. 10(g)–10(i)], and if they are of different amplitude ($s_1 \neq s_2$) the symmetry is $P2_1am$. Note that the displacement amplitudes in Fig. 10 have been artificially increased for clarity, so the displacement patterns shown should be viewed as the symmetry-allowed displacements, not the actual patterns obtained in relaxed structures. The relative contributions of the different displacement types to the total stripe distortion amplitude (as well as the amplitude itself) are determined from DFT + U structural relaxations.

To make this point clear, Table VI shows the decomposition of the stripe distortion into physically intuitive displacements, obtained from DFT + U structural relaxations with the symmetry constrained to several isotropy subgroups of Σ_2. It is clear from Table VI that the total distortion amplitude as well as the relative contribution of the different displacement types depends on the magnetic order. Starting with the *Pmam* structure with FM order, the largest contribution to the stripe distortion is the apical oxygen displacements in the SmO layer, followed by the O_{eq} and Sm displacements [thus, the displacement pattern in the relaxed structure looks most similar to Fig. 10(a), with the symmetry-allowed displacements in 10(b) and 10(c) having negligible amplitudes]. In contrast, the stripe distortion in the *Pmam* structure with A-AFM order has a much larger amplitude, and the relative contributions

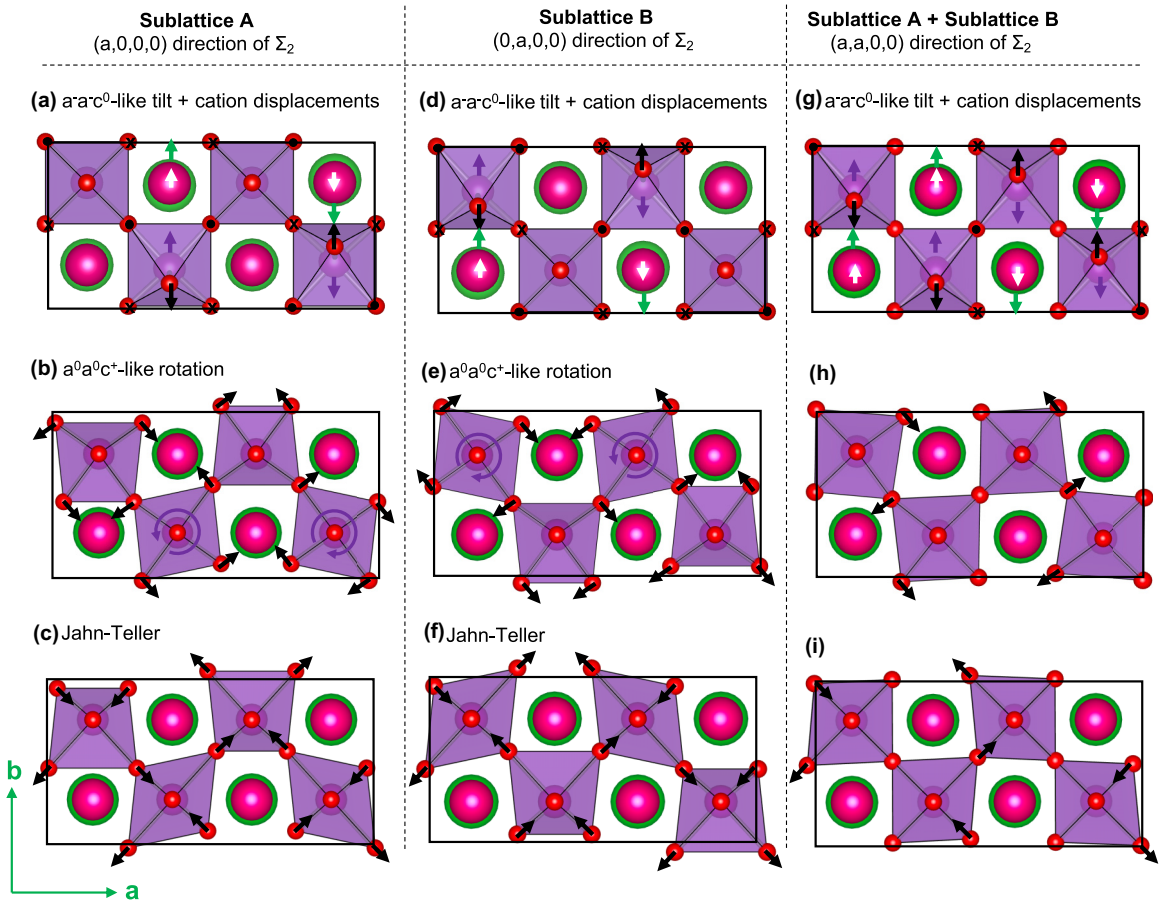

FIG. 10. Atomic displacements that contribute to the stripe distortion. The left column shows distortions present on sublattice A only: (a) $a^-a^-c^0$ octahedral tiltlike distortion and cation displacements, (b) $a^0a^0c^+$ octahedral rotationlike distortion, and (c) Jahn-Teller distortion. These distortions transform like the $(a, 0, 0, 0)$ direction of Σ_2 and establish a structure with symmetry *Pmam*. The middle column shows distortions on sublattice B only: (d) $a^-a^-c^0$ octahedral tiltlike distortion and cation displacements, (e) $a^0a^0c^+$ octahedral rotationlike distortion, and (f) Jahn-Teller distortion, which transform like the $(0, a, 0, 0)$ direction of Σ_2 and establish a different *Pmam* domain. The right column (g)–(i) shows the case where equal amplitudes of these distortions are present on both sublattices, which yields structures that transform like the $(a, a, 0, 0)$ direction of Σ_2 (symmetry *Pbam*). If the distortion amplitudes on the two sublattices are different [the $(a, b,0,0)$ direction of Σ_2], then the $P2_1am$ structure is established. Displacements of the oxygen atoms are indicated by black arrows, and the Mn, Sm, and Ba displacements are shown with purple, white, and green arrows, respectively. The amplitudes of all distortions are artificially increased for clarity.

of the displacement types are quite different, in particular, the $a^0a^0c^+$ rotationlike displacement now makes a significant contribution, and the Jahn-Teller distortion is also present. The remaining columns of Table VI show the decomposition of the stripe distortion for structures with *Pbam* and $P2_1am$ symmetry and different magnetic orders. There are variations in the total amplitude as well as the relative contributions of the different displacement types. However, for all structural symmetries and magnetic orders, the $a^-a^-c^0$ tiltlike displacements and the cation displacements are present, while the $a^0a^0c^+$ rotationlike displacement and Jahn-Teller distortion only contribute in certain cases.

Finally, Table VI shows that the displacements on the Mn^{3+} sublattice (sublattice A) are much larger than those on the Mn^{4+} sublattice for both the $P2_1am$ A-AFM and CE-AFM phases. By definition, the Jahn-Teller distortion is only present on the Mn^{3+} sublattice, but why are the octahedral tiltlike and rotationlike displacements also larger? We can answer this question using the following crystal chemical argument. Once there is some amount of CO ($Mn^{3.5+\delta}/Mn^{3.5-\delta}$) the Mn ions are different sizes: the Shannon radii of Mn^{3+} and Mn^{4+} in octahedral coordination are 0.645 and 0.53, respectively. Recalling that the tolerance factor for an ABO_3 perovskite is $\tau = (r_A + r_O)/[\sqrt{2}(r_B + r_O)]$, we can then think about separate tolerance factors for the Mn^{3+} and Mn^{4+} sublattices. Since $r_{Mn3+} > r_{Mn4+}$, then $\tau_{Mn3+} < \tau_{Mn4+}$, rationalizing the larger amplitude of octahedral tiltlike and rotationlike distortions on the Mn^{3+} sublattice.

APPENDIX E: STRUCTURAL DECOMPOSITION AND ENERGY SURFACE CALCULATIONS

This Appendix provides more details on our methods for structural decomposition and energy surface calculations. These are related analyses because in a structural decomposition we take a distorted structure (either from DFT or from experiment) and decompose it into symmetry-adapted modes that transform like irreps of the high-symmetry reference

TABLE VI. Decomposition of the Σ_2 stripe distortion into physically intuitive displacements (coefficients $A_{i\Sigma_2}$ obtained from a structural decomposition) on sublattices A and B, obtained from DFT structural relaxations with several symmetries and magnetic orders. The decomposition of the stripe distortion obtained from the $P2_1am$ CE-AFM structure, already presented in Table III, is reproduced here for ease of comparison. For phases with CO, sublattice A (B) corresponds to the Mn^{3+} (Mn^{4+}) sublattice. The amplitudes are reported in the 40-atom crystallographic unit cell in Å.

		Pmam FM		*Pmam* A-AFM		*Pbam* FM		*Pbam* A-AFM		$P2_1am$ A-AFM		$P2_1am$ CE-AFM	
i	Distortion	$\tilde{s}_A$	$\tilde{s}_B$	$\tilde{s}_A$	$\tilde{s}_B$	$\tilde{s}_A$	$\tilde{s}_B$	$\tilde{s}_A$	$\tilde{s}_B$	$\tilde{s}_A$	$\tilde{s}_B$	$\tilde{s}_A$	$\tilde{s}_B$
1	Jahn-Teller (O_{eq})	0.0	0.0	0.11	0.0	0.01	0.01	0.02	0.02	0.16	0.03	0.24	0.02
2	$a^0a^0c^+$ (O_{eq}) $a^-a^-c^0$	0.04	0.0	0.27	0.0	0.06	0.06	0.15	0.15	0.33	0.05	0.46	0.06
3	O_{ap} (Sm layer)	0.16	0.0	0.36	0.0	0.23	0.23	0.30	0.30	0.43	0.25	0.53	0.26
4	O_{ap} (Ba layer)	0.02	0.0	0.0	0.0	0.03	0.03	0.04	0.04	0.02	0.07	0.05	0.08
5	O_{eq}	0.08	0.0	0.18	0.0	0.14	0.14	0.18	0.18	0.23	0.19	0.28	0.21
6	Mn	0.01	0.0	0.06	0.0	0.01	0.01	0.02	0.02	0.11	0.00	0.20	0.00
7	Sm	0.09	0.0	0.06	0.0	0.08	0.08	0.08	0.08	0.01	0.09	0.05	0.07
8	Ba	0.01	0.0	0.04	0.0	0.01	0.01	0.02	0.02	0.09	0.01	0.13	0.01
	Total	0.21	0.0	0.50	0.0	0.37	0.37	0.40	0.40	0.63	0.34	0.83	0.36

structure $P4/mmm$, while for the energy surface calculations we start with $P4/mmm$ and freeze in symmetry-adapted modes to create distorted structures.

Let $\mathbf{R}_{P4/mmm}$ and $\mathbf{R}_{LS}$ be vectors containing the atomic positions for the high-symmetry reference structure $P4/mmm$ and a low-symmetry (LS) structure (which could be $P2_1am$, $Cmmm$, etc.). We can then write

$$\mathbf{R}_{\mathrm{LS}} = \mathbf{R}_{P4/mmm} + \mathbf{u}, \tag{E1}$$

where $\mathbf{u}$ is a vector containing displacements of the atoms from their high-symmetry positions. To perform a symmetry analysis of the displacements, $\mathbf{u}$ can be decomposed into symmetry-adapted modes that transform like irreps of $P4/mmm$. For the $P2_1am$ ground-state structure $\mathbf{u}$ can be written as

$$\begin{aligned}\mathbf{u} = &\sum_{i=1}^{2} A_{i\Gamma_1^+}\mathbf{e}_{i\Gamma_1^+} + \sum_{i=1}^{7} A_{i\Gamma_5^-}\mathbf{e}_{i\Gamma_5^-} + \sum_{i=1}^{6} A_{iM_5^-}\mathbf{e}_{iM_5^-} \\ &+ \sum_{i=1}^{2} A_{iM_4^+}\mathbf{e}_{iM_4^+} + \sum_{i=1}^{1} A_{iM_1^+}\mathbf{e}_{iM_1^+} + \sum_{i=1}^{16} A_{i\Sigma_2}\mathbf{e}_{i\Sigma_2}.\end{aligned} \tag{E2}$$

Here, $\mathbf{e}_{i\tau}$ labels a normalized symmetry-adapted mode that transforms like the irrep τ of $P4/mmm$, where $\tau = \{\Gamma_1^+, \Gamma_5^-, M_5^-, M_4^+, M_1^+, \Sigma_2\}$. The index i sums over the number of modes that transform like each irrep, where the total number of modes is equal to the total number of free atomic positions in the structure (for $P2_1am$, there are 33). Note that we do not discuss the Γ_1^+ and M_1^+ modes in the main text because Γ_1^+ describes strain modes that maintain the $P4/mmm$ symmetry, and the M_1^+ mode has zero amplitude in all structures that we consider. The coefficient $A_{i\tau} = \mathbf{u}\cdot\mathbf{e}_{i\tau}$ gives the amplitude that mode $\mathbf{e}_{i\tau}$ contributes to the total distortion amplitude $|\mathbf{u}|$. The amplitudes reported in Table I are obtained by summing over all modes i that transform like a given irrep τ, that is, $A_\tau = \sqrt{\sum_i A_{i\tau}^2}$.

To calculate the energy surfaces presented in Fig. 4, we start with the high-symmetry reference structure $P4/mmm$ and freeze in increasing amplitudes of the symmetry-adapted modes described above. As a concrete example, to calculate the M_5^- energy surface shown in the left panel of Fig. 4, we construct j structures (with symmetry *Pmam*)

$$\mathbf{R}_{Pmam,j} = \mathbf{R}_{P4/mmm} + B_j\mathbf{e}_{M_5^-}, \tag{E3}$$

where B_j is the mode amplitude frozen into the jth structure,

$$\mathbf{e}_{M_5^-} = \frac{1}{N_{M_5^-}}\sum_{i=1}^{6} A_{iM_5^-}\mathbf{e}_{iM_5^-} \tag{E4}$$

is the normalized sum of all modes that transform like M_5^-, and

$$N_{M_5^-} = \sqrt{\sum_{i=1}^{6} A_{iM_5^-}^2} \tag{E5}$$

is the normalization coefficient. From Eq. (E4), it is clear that to construct $\mathbf{e}_{M_5^-}$, values for the $A_{iM_5^-}$ coefficients are needed. We obtain these from structural decompositions of the

TABLE VII. Coefficients $A_{iM_5^-}$ obtained from structural decomposition of several structures of different symmetry that contain the M_5^- distortion. Note that for *Pmam* and *Cmmm*, the coefficients and the same regardless of whether FM or A-AFM order is imposed, while for $P2_1am$ there are small differences between the results with CE-AFM and A-AFM orders (listed separately). The coefficients are in units of Å, and are given for a 20-atom cell for *Pmam* and *Cmmm* and a 40-atom cell for $P2_1am$.

i	Displacement	*Pmam*	*Cmmm*	$P2_1am$ CE-AFM	$P2_1am$ A-AFM
1	O_{ap} (Sm layer)	0.36	0.46	0.57	0.55
2	O_{ap} (Ba layer)	0.15	0.17	0.24	0.23
3	O_{eq}	0.34	0.40	0.56	0.53
4	Mn	0.01	0.01	0.02	0.01
5	Sm	0.09	0.12	0.11	0.12
6	Ba	0.03	0.03	0.02	0.02
$N_{M_5^-}$	total	0.53	0.65	0.84	0.80

TABLE VIII. Coupled structural, OO, and CE-AFM domains in the $P2_1am$ CE-AFM ground state of $SmBaMn_2O_6$. There are 16 structural domains, 8 OO domains, and 16 magnetic domains, so each OO domains couples to two structural and two magnetic domains. Here only 8 magnetic domains are shown, the other 8 can be reached by flipping the signs on both magnetic order parameters. Domains in the two orthorhombic twins are distinguished by the space-group setting ($P2_1am$ and $Pb2_1m$).

Domain	M_5^-	M_4^+	Σ_2	Γ_5^-	Space group	OO	$\mathbf{L}_{\mathrm{CE}}$	$\mathbf{X}_{\mathrm{CE}}$
1	(0,T)	$-Q_b$	(b, -a, 0, 0)	(-P,-P)	$P2_1am$	(0,-σ,0,0)	(0,0,0,L)	(0,-X)
2	(0,T)	$-Q_b$	(-b, a, 0, 0)	(-P,-P)	$P2_1am$	(0,σ,0,0)	(0,0,0,L)	(0,X)
3	(0,T)	Q_b	(a, -b, 0, 0)	(P, P)	$P2_1am$	(σ,0,0,0)	(0,0,L,0)	(X,0)
4	(0,T)	Q_b	(-a, b, 0, 0)	(P, P)	$P2_1am$	(-σ,0,0,0)	(0,0,L,0)	(-X,0)
5	(0,-T)	$-Q_b$	(b, a, 0, 0)	(P, P)	$P2_1am$	(0,σ,0,0)	(0,0,0,L)	(0,X)
6	(0,-T)	$-Q_b$	(-b, -a, 0, 0)	(P, P)	$P2_1am$	(0,-σ,0,0)	(0,0,0,L)	(0,-X)
7	(0,-T)	Q_b	(a, b, 0, 0)	(-P,-P)	$P2_1am$	(σ,0,0,0)	(0,0,L,0)	(X,0)
8	(0,-T)	Q_b	(-a, -b, 0, 0)	(-P,-P)	$P2_1am$	(-σ,0,0,0)	(0,0,L,0)	(-X,0)
9	(T,0)	Q_b	(0, 0, a, b)	(P,-P)	$Pb2_1m$	(0,0,σ,0)	(L,0,0,0)	(X,0)
10	(T,0)	Q_b	(0, 0,-a,-b)	(P,-P)	$Pb2_1m$	(0,0,-σ,0)	(L,0,0,0)	(-X,0)
11	(T,0)	$-Q_b$	(0, 0, b, a)	(-P, P)	$Pb2_1m$	(0,0,0,σ)	(0,L,0,0)	(0,X)
12	(T,0)	$-Q_b$	(0, 0, -b, -a)	(-P, P)	$Pb2_1m$	(0,0,0,-σ)	(0,L,0,0)	(0,-X)
13	(-T,0)	Q_b	(0, 0, a, -b)	(-P, P)	$Pb2_1m$	(0,0,σ,0)	(L,0,0,0)	(X,0)
14	(-T,0)	Q_b	(0, 0, -a, b)	(-P, P)	$Pb2_1m$	(0,0,-σ,0)	(L,0,0,0)	(-X,0)
15	(-T,0)	-Q_b	(0, 0, b, -a)	(P,-P)	$Pb2_1m$	(0,0,0,-σ)	(0,L,0,0)	(0,-X)
16	(-T,0)	-Q_b	(0, 0, -b, a)	(P,-P)	$Pb2_1m$	(0,0,0,σ)	(0,L,0,0)	(0,X)

DFT + U-relaxed structures. Table VII shows the coefficients $A_{iM_5^-}$ obtained from structural decompositions of DFT + U-relaxed structures with $Pmam$, $Cmmm$, and $P2_1am$ symmetry. There are slight variations between the relative contributions of the different $A_{iM_5^-}$ depending on the structural symmetry. However, the differences are small enough that the resulting M_5^- energy surface does not depend much on which $A_{iM_5^-}$ we use in the calculation. We choose to use the $A_{iM_5^-}$ in Table VII obtained from the $P2_1am$ A-AFM structural relaxation (the reason for this choice will become clear below).

We can write analogous expressions for the symmetry-adapted modes that we use to compute the other energy surfaces. The question of which coefficients $A_{i\Sigma_2}$ to use in the calculation of the Σ_2 energy surface is more complicated for two reasons, both of which are evident from Table VI. Note that there are 16 such coefficients, 8 coming from the displacements on each sublattice (see Table VI). First, the relative contributions of the various $A_{i\Sigma_2}$ depend strongly on the structural symmetry, for example, the modes that correspond to the Jahn-Teller and $a^0a^0c^+$ rotationlike distortion only contribute in certain structures. Second, even within the same structural symmetry, the relative sizes of the $A_{i\Sigma_2}$ coefficients depend on the magnetic order imposed in the structural relaxation. Thus, we must choose which set of $A_{i\Sigma_2}$ from Table VI to use in the construction of $\mathbf{e}_{\Sigma_2}$, and perform the energy surface calculations with the same magnetic order as was used in the calculation of the $A_{i\Sigma_2}$ coefficients.

Since the primary goal of our energy surface calculations is to understand the instabilities of $P4/mmm$ as well as the coupling terms that stabilize the ground state, we choose to construct $\mathbf{e}_{\Sigma_2}$ using coefficients $A_{i\Sigma_2}$ from a $P2_1am$ structural relaxation because this is the form of the distortion that couples to CO. As is evident from Table VI, the $A_{i\Sigma_2}$ obtained from relaxation with $P2_1am$ symmetry and A-AFM and CE-AFM orders are similar (but not identical). We choose to use the A-AFM coefficients (and calculate all energy surfaces in Fig. 4 with A-AFM) because this allows us to focus on the energetics of the coupled structural distortions, without the additional energy contribution from the coupling between CO and CE-AFM. However, our conclusions do not depend on this choice, see the Supplemental Material [28] for energy surfaces calculated using other choices of $A_{i\Sigma_2}$.

APPENDIX F: FREE-ENERGY EXPANSION AND DOMAINS

For simplicity, the free-energy expansions in the main text are given for one orthorhombic twin domain. With the full multidimensional order parameters, which are required to treat both twins at the same time, the coupling terms between structural order parameters in Eqs. (2)–(4) are

$$F_{tss} = \delta_{tss}(T_1 s_3 s_4 - T_2 s_1 s_2), \tag{F1}$$

$$F_{bss} = \delta_{bss} Q_b \left(s_1^2 - s_2^2 + s_3^2 - s_4^2\right), \tag{F2}$$

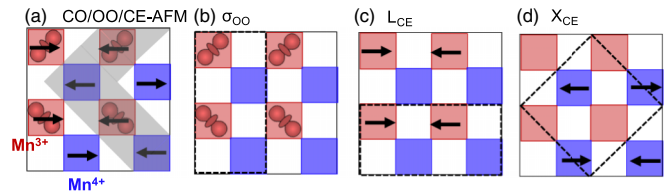

FIG. 11. CO, OO, and CE-AFM order parameters. (a) The CO/OO/CE-AFM phase with Mn^{3+} and Mn^{4+} sites colored red and blue, respectively. The order parameters are shown individually for (b) OO, (c) magnetic order L_{CE} on the Mn^{3+} sublattice, and (d) magnetic order X_{CE} on the Mn^{4+} sublattice. The black dashed lines indicate the unit cell for each order parameter.

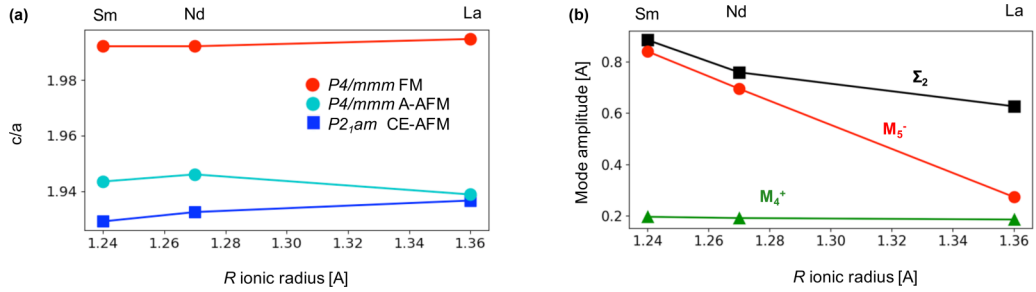

FIG. 12. Evolution of the crystal structure of $R\mathrm{BaMn_2O_6}$ with change to the rare-earth R^{3+} ionic radius: (a) c/a ratio for the $P2_1am$ CE-AFM and the $P4/mmm$ FM and A-AFM phases, and (b) the symmetry-adapted mode amplitudes for the $P2_1am$ CE-AFM phase.

and

$$F_{tbp} = \delta_{tbp}[T_1 Q_b(P_1 - P_2) + T_2 Q_b(P_1 + P_2)]. \quad \text{(F3)}$$

These free-energy expansions are used to derive the order-parameter directions of the $P2_1am$ structural domains shown in Table VIII.

Figure 11(a) summarizes the relationship between the CO, OO, and CE-AFM order parameters. The $d_{x^2-r^2}/d_{y^2-r^2}$ OO [Fig. 11(b)], which we denote by the order parameter $\sigma_{\mathrm{OO}} = (\sigma_1, \sigma_2, \sigma_3, \sigma_4)$, transforms like the $(a, 0, 0, 0)$ direction of Σ_2 and thus couples bilinearly to the stripe distortion. The two magnetic order parameters that describe the CE-AFM state are shown in Figs. 11(c) and 11(d). The first, $L_{\mathrm{CE}} = (L_1, L_2, L_3, L_4)$, transforms like the (0,0,a,0) direction of the $m\Sigma_1$ irrep and describes the magnetic ordering on the $\mathrm{Mn^{3+}}$ sublattice, while the second, $X_{\mathrm{CE}} = (X_1, X_2)$, transforms like the ($a$,0) direction of the $mX_1^+ - mX_2^+$ irrep and describes the magnetic ordering on the $\mathrm{Mn^{4+}}$ sublattice (the m indicates *magnetic* irreps, where time reversal changes the sign of all magnetic moments [49]). The magnetic point group established by CE-AFM with spins lying in the ab plane is $P_b mc2_1$.

Note that in the main text we treated L_{CE} and X_{CE} as two- and one-dimensional order parameters, respectively, which restricted that analysis to one orthorhombic twin. With the full order parameters presented here, the free-energy expansion given in Eq. (6) then becomes

$$\begin{aligned} F_{cL} = {} & \eta_{cL} Q_{\mathrm{CO}}\left(L_1^2 - L_2^2 + L_3^2 - L_4^2\right) + \eta_{cX} Q_{\mathrm{CO}}\left(X_1^2 - X_2^2\right) \\ & + \eta_{\sigma LX}\left(\sigma_1 L_3 X_1 + \sigma_3 L_1 X_1 + \sigma_2 L_4 X_2 + \sigma_4 L_2 X_2\right) \\ & + \eta_{LX}\left(L_1^2 - L_2^2 + L_3^2 - L_4^2\right)\left(X_1^2 - X_2^2\right). \end{aligned} \quad \text{(F4)}$$

This expansion is used to determine the OO and CE-AFM domains that couple to the structural domains of $P2_1am$ (see Table VIII).

APPENDIX G: PHASE CONTROL WITH CHEMICAL SUBSTITUTION

Given that $\mathrm{SmBaMn_2O_6}$ has a $P2_1am$ CE-AFM ground state, and $\mathrm{LaBaMn_2O_6}$ is a FM metal, chemical substitution ($\mathrm{Sm_{1-x}La_xBaMn_2O_6}$) may be an alternative strategy to tune the material such that these two ground states compete. We note that this strategy has been tried experimentally, and while phase separation into FM and CO insulating regions was observed, no CMR effect was detected [52].

One of the main effects of chemical substitution is to change the average R^{3+} ionic radius. We can access this effect just by varying the R cation in $R\mathrm{BaMn_2O_6}$, which gives access to the essential physics but is simpler than including dopants in our calculations. Figure 12(a) shows the c/a ratio for a few selected structures with R = Sm, Nd, and La. As discussed in the main text, the c/a ratio is different depending on whether the spins are FM- or AFM- coupled along the c axis: for FM coupling $c/a \approx 1.98$, while for the AFM coupling, $c/a \approx 1.93$. The c/a ratio hardly changes as we vary the ionic radius of R. This shows that doping La to form $\mathrm{Sm_{1-x}La_xBaMn_2O_6}$ may be a less effective way of tuning the ground state than epitaxial strain because it does not change the c/a ratio which couples strongly to the magnetic state.

Figure 12(b) shows the symmetry-adapted mode amplitudes for the $P2_1am$ CE-AFM phase, again for R = Sm, Nd, and La. The most noticeable feature is that the amplitude of the M_5^- octahedral tilt reduces significantly, which reflects that the tolerance factor is getting closer to 1. The Σ_2 stripe distortion also decreases somewhat. However, the amplitude of the M_4^+ breathing distortion, which directly couples to the magnetic states, hardly changes.

[1] M. Imada, A. Fujimori, and Y. Tokura, Rev. Mod. Phys. **70**, 1039 (1998).
[2] E. Dagotto, Science **309**, 257 (2005).
[3] Y. Tokura, Rep. Prog. Phys. **69**, 797 (2006).
[4] E. Dagotto, *Nanoscale Phase Separation and Colossal Magnetoresistance: The Physics of Manganites and Related Compounds*, Vol. 136 (Springer, New York, 2003).
[5] J. Seidel, R. K. Vasudevan, and N. Valanoor, Adv. Electron. Mater. **2**, 1500292 (2016).
[6] F.-T. Huang and S.-W. Cheong, Nat. Rev. Mater. **2**, 17004 (2017).
[7] J. Seidel, L. W. Martin, Q. He, Q. Zhan, Y.-H. Chu, A. Rother, M. Hawkridge, P. Maksymovych, P. Yu, M. Gajek *et al.*, Nat. Mater. **8**, 229 (2009).
[8] D. Meier, J. Seidel, A. Cano, K. Delaney, Y. Kumagai, M. Mostovoy, N. A. Spaldin, R. Ramesh, and M. Fiebig, Nat. Mater. **11**, 284 (2012).
[9] Y. S. Oh, X. Luo, F.-T. Huang, Y. Wang, and S.-W. Cheong, Nat. Mater. **14**, 407 (2015).

[10] E. Y. Ma, Y.-T. Cui, K. Ueda, S. Tang, K. Chen, N. Tamura, P. M. Wu, J. Fujioka, Y. Tokura, and Z.-X. Shen, Science **350**, 538 (2015).

[11] E. Y. Ma, B. Bryant, Y. Tokunaga, G. Aeppli, Y. Tokura, and Z.-X. Shen, Nat. Commun. **6**, 7595 (2015).

[12] S. Farokhipoor, C. Magén, S. Venkatesan, J. Íñiguez, C. J. Daumont, D. Rubi, E. Snoeck, M. Mostovoy, C. De Graaf, A. Müller *et al.*, Nature (London) **515**, 379 (2014).

[13] H. T. Hirose, J.-i. Yamaura, and Z. Hiroi, Sci. Rep. **7**, 42440 (2017).

[14] H. Noad, P. Wittlich, J. Mannhart, and K. A. Moler, J. Supercond. Novel Magn. **32**, 821 (2018).

[15] D. Akahoshi, M. Uchida, Y. Tomioka, T. Arima, Y. Matsui, and Y. Tokura, Phys. Rev. Lett. **90**, 177203 (2003).

[16] T. Nakajima, H. Kageyama, H. Yoshizawa, K. Ohoyama, and Y. Ueda, J. Phys. Soc. Jpn. **72**, 3237 (2003).

[17] D. Akahoshi, Y. Okimoto, M. Kubota, R. Kumai, T. Arima, Y. Tomioka, and Y. Tokura, Phys. Rev. B **70**, 064418 (2004).

[18] T. Arima, D. Akahoshi, K. Oikawa, T. Kamiyama, M. Uchida, Y. Matsui, and Y. Tokura, Phys. Rev. B **66**, 140408(R) (2002).

[19] D. Morikawa, K. Tsuda, Y. Maeda, S. Yamada, and T.-h. Arima, J. Phys. Soc. Jpn. **81**, 093602 (2012).

[20] S. Yamada, Y. Maeda, and T.-h. Arima, J. Phys. Soc. Jpn. **81**, 113711 (2012).

[21] H. Sagayama, S. Toyoda, K. Sugimoto, Y. Maeda, S. Yamada, and T. Arima, Phys. Rev. B **90**, 241113(R) (2014).

[22] K. Yamauchi, J. Phys. Soc. Jpn. **82**, 043702 (2013).

[23] Y. Tokunaga, T. Lottermoser, Y. Lee, R. Kumai, M. Uchida, T. Arima, and Y. Tokura, Nat. Mater. **5**, 937 (2006).

[24] C. Ma, Y. Lin, H. Yang, H. Tian, L. Shi, J. Zeng, and J. Li, Adv. Mater. **27**, 6328 (2015).

[25] K. Yamauchi and S. Picozzi, J. Phys. Soc. Jpn. **82**, 113703 (2013).

[26] E. O. Wollan and W. C. Koehler, Phys. Rev. **100**, 545 (1955).

[27] J. B. Goodenough, Phys. Rev. **100**, 564 (1955).

[28] See Supplemental Material at http://link.aps.org/supplemental/10.1103/PhysRevB.100.195129 for additional results including spin density isosurfaces, density of states, additional energy surface and epitaxial strain calculations, lattice parameters, and symmetry-adapted mode amplitudes for all structures considered in the main text, and all subgroups of the Σ_2 irrep.

[29] A. Glazer, Acta Crystallogr., Sect. B: Struct. Crystallogr. Cryst. Chem. **28**, 3384 (1972).

[30] B. H. Savitzky, I. El Baggari, A. S. Admasu, J. Kim, S.-W. Cheong, R. Hovden, and L. F. Kourkoutis, Nat. Commun. **8**, 1883 (2017).

[31] I. El Baggari, B. H. Savitzky, A. S. Admasu, J. Kim, S.-W. Cheong, R. Hovden, and L. F. Kourkoutis, Proc. Natl. Acad. Sci. USA **115**, 1445 (2018).

[32] F. Zhong and Z. D. Wang, Phys. Rev. B **61**, 3192 (2000).

[33] J. Ribeiro, Phys. B (Amsterdam) **492**, 55 (2016).

[34] E. Bousquet, M. Dawber, N. Stucki, C. Lichtensteiger, P. Hermet, S. Gariglio, J.-M. Triscone, and P. Ghosez, Nature (London) **452**, 732 (2008).

[35] N. A. Benedek and C. J. Fennie, Phys. Rev. Lett. **106**, 107204 (2011).

[36] J. M. Rondinelli and C. J. Fennie, Adv. Mater. **24**, 1961 (2012).

[37] E. A. Nowadnick and C. J. Fennie, Phys. Rev. B **94**, 104105 (2016).

[38] K. Du, K. Zhang, S. Dong, W. Wei, J. Shao, J. Niu, J. Chen, Y. Zhu, H. Lin, X. Yin *et al.*, Nat. Commun. **6**, 6179 (2015).

[39] Y. Li, S. Dong, and S.-P. Kou, Phys. Rev. B **93**, 085139 (2016).

[40] A. Asamitsu, Y. Tomioka, H. Kuwahara, and Y. Tokura, Nature (London) **388**, 50 (1997).

[41] J. Stankiewicz, J. Sesé, J. García, J. Blasco, and C. Rillo, Phys. Rev. B **61**, 11236 (2000).

[42] P. G. Radaelli, D. E. Cox, M. Marezio, and S.-W. Cheong, Phys. Rev. B **55**, 3015 (1997).

[43] R. J. Goff and J. P. Attfield, Phys. Rev. B **70**, 140404(R) (2004).

[44] J. Blasco, J. Garcia, J. De Teresa, M. Ibarra, J. Perez, P. Algarabel, C. Marquina, and C. Ritter, J. Phys.: Condens. Matter **9**, 10321 (1997).

[45] G. Kresse and J. Hafner, Phys. Rev. B **47**, 558 (1993).

[46] G. Kresse and D. Joubert, Phys. Rev. B **59**, 1758 (1999).

[47] J. P. Perdew, A. Ruzsinszky, G. I. Csonka, O. A. Vydrov, G. E. Scuseria, L. A. Constantin, X. Zhou, and K. Burke, Phys. Rev. Lett. **100**, 136406 (2008).

[48] A. I. Liechtenstein, V. I. Anisimov, and J. Zaanen, Phys. Rev. B **52**, R5467(R) (1995).

[49] H. Stokes, D. Hatch, and B. Campbell. ISOTROPY Software Suite, http://stokes.byu.edu/isotropy.html.

[50] K. Momma and F. Izumi, J. Appl. Crystallogr. **41**, 653 (2008).

[51] S. Yamada, H. Sagayama, K. Higuchi, T. Sasaki, K. Sugimoto, and T. Arima, Phys. Rev. B **95**, 035101 (2017).

[52] Y. Ueda and T. Nakajima, Prog. Solid State Chem. **35**, 397 (2007).